Spring 2014

Investigation of electrical and impact properties of carbon fiber textile composites

Bryne Berry
University of Iowa

INVESTIGATION OF ELECTRICAL AND IMPACT PROPERTIES OF CARBON FIBER TEXTILE COMPOSITES

by

Bryne Berry

A thesis submitted in partial fulfillment
of the requirements for the Master of
Science degree in Mechanical Engineering
in the Graduate College of
The University of Iowa

May 2014

Thesis Supervisor: Professor Olesya I. Zhupanska

Graduate College
The University of Iowa
Iowa City, Iowa

CERTIFICATE OF APPROVAL

MASTER'S THESIS

This is to certify that the Master's thesis of

Bryne Berry

has been approved by the Examining Committee
for the thesis requirement for the Master of Science
degree in Mechanical Engineering at the May 2014 graduation.

Thesis Committee: _____
Olesya I. Zhupanska, Thesis Supervisor

_____
Albert Ratner

_____
Hiroyuki Sugiyama

To My Loving Family Whom I Adore

ACKNOWLEDGEMENTS

I would like to thank Yeqing Wang, Brandon Demerath, Matias Perret, Austin Krebill, and Philip Deierling for their extensive help with this the thesis. This work is partially supported by the National Science Foundation under Grant Number EPS-1101284. Any opinions, findings, and conclusions or recommendations expressed in this work are those of the author and do not necessarily reflect the views of the National Science Foundation. I would also like to thank the Iowa Space Grant Consortium (ISGC) for partial funding. I would also like to thank Dr. Zhupanska for her guidance.

TABLE OF CONTENTS

LIST OF TABLES

LIST OF FIGURES

CHAPTER 1
INTRODUCTION

1.1 Literature Review

This literature review will focus on the characteristics, mechanical behavior, basic terminology, manufacturing, and applications of textile reinforced fiber composites. In addition, literature will be gathered about damage tolerance and damage sensing in textile composites.

1.1.1 Characteristics

Composites are engineered materials made from two or more constituent materials with significantly different mechanical properties and which remain separate and distinct within the finished structure. The composite is composed of constituent materials that include a reinforcement and a matrix. In textile composites, the fiber reinforcement is made through textile techniques such as braiding, weaving, and knitting which gives rise to the term textile composites (Paracha, 2010).

Textile composites have become popular due to their low material cost and labor requirements compared to traditional unidirectional prepreg composites. They also provide high strength-to weight and stiffness-to-weight ratios compared with the use of randomly orientated reinforcements (Bakar, 2013). Woven-fabric composite laminates offer a number of attractive properties compared to their unidirectional-tape counterparts such as lower production costs, better drapability, good resistance to fracture and transverse rupture due to weaving resistance, and high impact strength (Ullah et al, 2011).

At the microscopic level, woven (textile) composites (irrespective of their fiber

architecture) are assembled from bundles of parallel fibers embedded in a matrix material that is usually polymeric and has a much lower modulus, and is usually assumed to be homogeneous and isotropic (Long, 2005).

What makes a composite a textile is the textile architecture of the reinforcement constituent that is used to carry the load. The mechanical properties of woven fabrics are governed by: (a) weave parameters such as an architecture pattern, yarn size, yarn spacing length, fiber crimp angle and volume fraction of fiber bundles, and (b) laminate parameters such as stacking orientation and overall fiber volume fraction (Bakar, 2013).

1.1.2 Mechanical Behavior

The mechanical properties of woven fabrics are governed by: (a) weave parameters such as an architecture pattern, yarn size, yarn spacing length, fiber crimp angle and volume fraction of fiber bundles, and (b) laminate parameters such as stacking orientation and overall fiber volume fraction (Bakar, 2013).

The four main factors that govern the fiber's contribution are the basic mechanical property to the fiber itself, the surface interaction of fiber and resin or the interface, the amount of fiber in the composite (the fiber volume fraction), and the orientation of the fibers in the composite Reinforcements can be 1-D, 2-D, or 3-D (Paracha, 2010).

Fibers provide their greatest strength when they are perfectly straight, thus the frequent over-and under-crossing of the threads induces a slight curvature in the fibers, or "pre-buckling" and consequently reduces its strength and mechanical properties (Balaguru, 2009).

1.1.3 Basic Terminology

Woven fabrics generally consist of two sets of yarns that are interlaced and lie

orthogonal to each other. The yarns that run along the length of the fabric are known as warp ends whilst the threads that run from one side to the other side of the fabric are weft picks (Bakar, 2013). In general, weave patterns are defined by a number notation such as 4X4, 5X3, and 2X2. The first number in the notation indicates the number of yarns that crossed ‘‘over’’, known as warp direction before it changes direction or known as weft direction (perpendicular yarns). The weaves are classified into three different basic styles: (a) Plain weave. (b) Twill weave. (c) Harness-Satin weaves (Bakar, 2013). Figure 1.1 shows the different weave types.

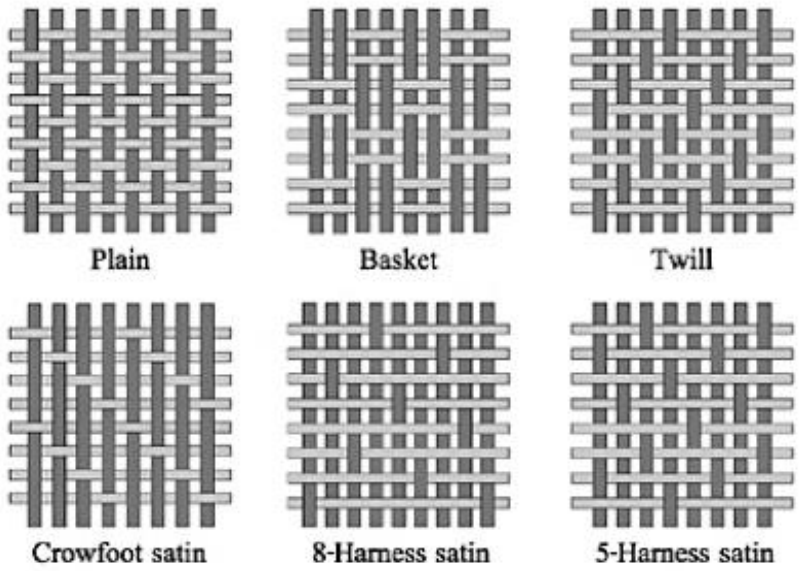

Figure 1.1: Basic Weave Types (Balaguru, 2009)

A plain weave is defined as a 1X1 weave and a twill weave is defined as a set of identical number of weave both under and over such as 2X2 and 4X4 twill weaves (Bakar, 2013). The plane weave (0/90) is the most common weave construction used and requires only four weaving yarns: two warps and two fills. For a simple plain-woven fabric, half of the fibers are in the warp (0) orientation and the other half is in the fill (90)

direction. It is highly interlaced and is consequently, very resistance to in-plane shear movement (Balaguru, 2009).

A Harness-Satin is referred as Harness, Satin, or Crowfoot, which refers to any number larger than 1, followed by X, and another larger number larger than 1. The most common satin harness used are Harness-Satin 8(8HS) and Harness- Satin 5(5HS) (Bakar, 2013).

The twill woven laminate shows a higher tensile modulus than the plain woven laminate as expected from a larger qm. The satin woven laminate having the largest qm, however, shows a lower tensile modulus. The tensile strength of the woven laminates increases with increasing qm (Kim, 2004).

1.1.4 Manufacturing Methods

In manufacturing textile composites, the matrix material can be introduced to the reinforcement before or after the reinforcement material is placed into the mold cavity or surface melding. There are several types of manufacturing processes: vacuum bag molding, pressure bag molding, autoclave molding, and resin transfer molding (RTF) (Paracha, 2010). The woven laminates and felt/resin composites can be fabricated by employing a vacuum infusion process as follows: liquid epoxy resin poured into a mold heated at 80 C and the stack of woven fabrics or the felt are placed in the mold. The resin-impregnated fibers are placed in vacuum for 20 and 5 min before and after the mold was closed, respectively. The resin was cured with a hydraulic hot press under a pressure of 0.5 MPa (Kim, 2004).

1.1.5 Applications

Plain weaves are typically used for flat laminates, printed circuit boards, narrow fabrics, molds and covering wood boats (Kim, 2004). Composite materials comprise more than 20% of a A380's airframe. Carbon fiber reinforced plastic, glass-fiber reinforced plastic and quartz-fiber reinforced plastic are used extensively in the wings, fuselage sections (the undercarriage and rear end of fuselage), tail surfaces, and doors (Paracha, 2010).

1.2 Damage Tolerance of Textile Composites

When it comes to damage, composites do not have the sufficient properties with respect to impact. For example, at room temperature, most composites are brittle and do not plastically deform. Instead, composites can only absorb energy elastically or in one of several different damage modes (McAndrew, 2009). When it comes to textile composites, damage accumulation is a complicated process, and development begins on the micro-scale with the fiber matrix debonding, the matrix cracking and the fiber failure (the micro-scale defines the arrangement of fibers in an impregnated yarn or fibrous ply). (Daggumati et al, 2010). Most troublesome is when no visible damage at the impacted surface is observed and is coupled with significant reduction in the composite's strength and stiffness. With its increasing application and use of composites in wind turbine blades to aircraft, being able to withstand damage and show visible signs of damage is critical.

Low velocity impact machines are used to measure damage for the study of damage tolerance of composites. Low velocity impact machines are equipped with a weighted indenter to fall freely due to gravity and impact a composite sample (Abrate, 1998). For low velocity impacts, a drop weight and tup assembly, which consists of a load cell connected to the tup, strikes the composite sample. The drop weight is set to a

user-desired height and allowed to fall freely and strike the sample. Prior to impact a velocity flag passes through the photogate allowing it to detect the velocity and record the impact velocity. The force the tup exerts on the composite is recorded through the impact through the load cell located in the tup. Textile composites could be subjected to large-deflection and can undergo bending and multiple impacts. These loads generate high local stresses and strains leading to complex damage modes due to heterogeneity and anisotropy of composite laminates (Ullah et all, 2011).

When identifying results of low impact velocity impacts of textile composites, it is seen that laminates can absorb the impact energy by different means including indentation (representative of local matrix crushing and local fiber breakage), delamination (inter-yarn fracture), split- ting (intra-yarn fracture) or fibers peeling on the non-impacted side (Daggumati et all, 2010). During low velocity impacts, the first type of damage is matrix cracking, which does not significantly change the overall stiffness of laminates. Even though the weave structure prevents the fiber bundles from migrating into the interply layer during fabrication, the deviation of fabric surface from planarity introduces macroscopic roughness, depending on the fabric thickness as well as the weaving patterns. Modes I and II interlaminar fractures toughness play important roles in determining the impact damage behavior of composites (Vieille, Benoit and Casado, 2013).

The second most common type of damage in low-velocity impact of textile composites is interlayer delamination. The delamination propagates through the interlayer leading to catastrophic failure of the composites (Kim, 2004). What is most concerning is that this damage is often non-visible. Delamination initiation in composite laminates is usually assessed by strength-based criteria; for instance, the maximum nominal stress, and quadratic strength criteria are used successfully for this purpose (Ullah et all, 2011).

The primary impact failure mechanisms are a very complex combination of energy absorption mechanisms such as delamination predominantly caused by modes I–II

interlaminar shear matrix cracking, and interlaminar fracture in terms of fiber fracture and kinking or splitting. The measurement of the specimen's indentation is typically used to assess the impact damage. In general, the indentation just after the impact (temporary indentation) is always higher than the indentation after relaxation of the impacted composite. Such relaxation effects can be neglected after 48 h to get the permanent indentation (Vieille, Benoit and Casado, 2013). Some damage is seen in Figure 1.2.

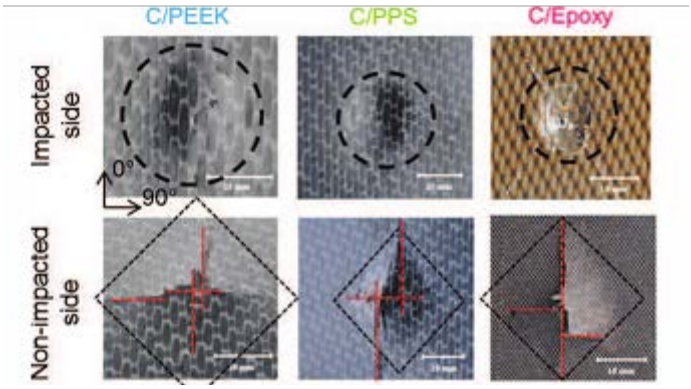

Figure 1.2: Impact Damage Patterns on Front and Back Sides of Specimens (Vieille, Benoit and Casado, 2013)

Fiber breakage occurs on the top surface due to large contact stresses and indentation effects and on the back surface as a result of bending stresses (McAndrew, 2009).

When the degree of fiber failure becomes severe enough, the final damage mode, penetration, occurs. This mode represents catastrophic failure as the impactor goes through the specimen completely (Richardson & Wisheart, 1996).

In identifying causes of damage in composites, parameters such as the fiber orientation, localized fiber spacing and packing often exhibit a wide statistical variation when evaluated on the micro-scale in a processed composite. The inhomogeneity of the stress field, coupled with the inhomogeneity of the strength properties of the reinforcing

elements, the matrix and the interface, lead to the gradual damage development in composites (Daggumati et all, 2010). In a bending scenario, a laminate experiences transverse shear and normal stresses resulting in the interlaminar delamination damage, because of their low through-thickness strength and stiffness (Ullah et all, 2011).

Once the material's stiffness has changed during low velocity impact tests, the profile of the force–displacement curve is unique to each material. Damage evolution results in significant reduction of in-service mechanical properties and can lead to loss of structural integrity of the composite (Vieille, Benoit and Casado, 2013).

Nevertheless, potential advantages of using woven fabrics as opposed to cross-ply unidirectional (UD) prepreg tapes are observed: woven-fabric laminates exhibit much higher critical strain energy release rates, or G_{IC} values (often more than 4–5 times) than the UD counter-parts. The unique features and advantageous failure mechanisms are identified: inherent roughness of the fabrics; the availability of matrix-rich regions between the fabrics; crack propagation along the undulating pattern of the yarns creating a large fracture surface area; and multiple crack fronts delamination. Thus, woven-ply laminates usually display reduced maximum loads, smaller damage areas, higher ductility and residual compression after impact (CAI) strength than UD-ply laminates, mainly because of higher mode II interlaminar fracture toughness (Vieille, Benoit and Casado, 2013).

Damage tolerance of composites can also be enhanced by improving interlaminar properties through toughening the matrix, inserting an interleaf layer, and reinforcing with three-dimensional braided and woven fabrics (Kim, 2004).

1.3 Damage Sensing in Textile Composites

Damage tolerant composite structures are critically important in the current and future aerospace systems as they rely more and more on fiber-reinforced polymer

composites. Non-destructive damage detection techniques are important when utilizing carbon fiber composites. Non-destructive evaluation (NDE) methods are required to visualize this three-dimensional (3D) internal deformation and damage behavior of composite structures. One of the recent methods is Micro-Computed Tomography (Micro CT) that can be used for imaging of material's internal structure based on X-ray absorption, which is related to the material density. This technique has been used to investigate micro cracking and delamination in composite laminates at micron-range level. Researchers found good behavioral correlation between the results obtained from simulations and Micro CT scans of deformed and undeformed woven glass and carbon fabric laminates (Ullah et all, 2011).

In addition, researchers have employed embedded damage detectors during the tensile test of a thermoplastic 5-harness satin weave composite under uni-axial static tensile load to determine the deformation behavior of the laminate inner layers that may vary from that of the surface layers, which are relatively more free to deform, compared to the inner layers. In one experiment, the embedded sensors were used to (a) determine local strain on the composite surface is quantified using the digital image correlation technique (LIMESS) together with surface mounted fiber optic sensors (Fiber Bragg Grating (FBG)); (b) embedded fiber optic sensors were used to obtain the maximum and minimum local strain values inside the laminate (Dugmatti et all, 2011). This is seen in Figure 1.4.

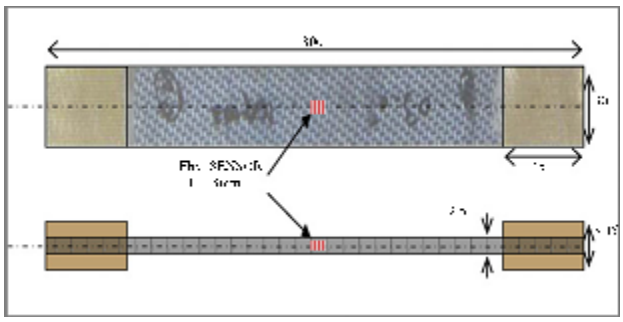

Figure 1.3: Sample with Fiber Bragg Grating Sensor (Dugmatti et all, 2010)

In addition, damage initiation can be detected using the acoustic emission (AE) technique during a tensile test. AE provides the damage initiation threshold and the critical stresses of the composite. In order to detect the location of the damage, microscopic analysis is used. In general, the characteristic failure mechanisms in fiber reinforced composites are initiated at the micro-level and result in a spontaneous release of elastic strain energy, which is dissipated as a wave that propagates from the failure source through the medium. AE measurement and data acquisition system (VALLEN) is used to detect the damage initiation stress followed by the microscopic analysis of the composite specimens for the inspection of damage locations (Dugmatti et all, 2010). However, a drawback with acoustic emission technique can only detect damage that is approximately one millimeter in length; a size larger than some of the damage experienced by composite materials (McAndrew, 2009).

Several techniques based on fracture-mechanics approach are employed in the finite element method (FEM) to simulate a delamination growth such as the J-integral, the virtual crack extension method and the virtual crack closure technique (VCCT). Fracture-mechanics analysis is limited in this respect since it neglects material's nonlinearity and requires the position of delamination crack to be known in advance (Ullah et all, 2011). In predicting techniques, modeling proves somewhat useful in mapping the fracture mechanics that the laminate undergoes after impact for fracture

mechanics. Cohesive-zone elements are able to predict both the onset and growth of delamination combining the strength- and fracture-based approaches in a single finite-element model without preliminary knowledge of a crack's location and propagation direction. However, application of cohesive-zone elements to model progressive delamination in composite structures poses numerical difficulties related to the proper definition of stiffness of the interface layer, the requirement of highly refined finite-element meshes, and convergence difficulties associated with a softening behavior of the interface material (Ullah et all, 2011).

Nevertheless, utilizing the composite's damage sensing properties where the material itself serves as the damage sensor leads to the concept of multifunctionality where the composite possess concurrent and superior mechanical characteristics and damage sensing capabilities. Using changes in electrical resistance to correlate impact damage within a composite is one of the motivating factors for this thesis.

Researchers in the past have used the electrical characterization of the carbon fiber polymer matrix composites in an attempt to monitor changes in the electric resistance and electric field that occur as a result of impact and other mechanical damage. Utilizing the composite's natural electrical conductivity as a way to detect damage offers an alternative to other damage-sensing techniques by exploiting its electrical conductivity instead. The basic principle of the self-sensing method is that the damages due to carbon fiber breakage or delamination in the laminate will cause an increase in electrical resistance, resulting in voltage change in the damaged region (Sevkat et all, 2008)

In addition to providing strength and stiffness, the carbon fibers of a carbon fiber reinforced polymer (CFRP) laminate are electrically conductive. Carbon fibers are intrinsically electrically conductive, having a typical resistivity of 1.5×10^{-5} m, while the epoxy matrix is an effective insulator having resistivity $\sim 10^{20}$ m (Weber and Schwartz, 2001). However, many synthetic fibers that are used in the textile fabrics are insulating materials with resistivity of order of 10^{15} cm (Safarova and Greger, 2010).

The conductive fibers constitute a conductive network that allows the composite as a whole to be conductive, even though the polymer matrix material is non-conductive. Thus damage changes the electrical resistance of the composite (McAndrew, 2009).

The through-thickness conductivity decreases due to both delamination and fiber-matrix debonding. Delamination decreases the conductivity since it separates fibers of adjacent laminae (Chung, 2007), while fiber-matrix debonding decreases the conductivity due to the additional resistance of the new space between the fibers and the matrix (Motahhari, Cao, & Cameron, 2000). Since the conductivity of a CFRP laminate changes with damage, measuring the electrical conductivity of such a composite provides a meaningful method of damage sensing.

The resistance method is employed in this research and previous research and gets its name from the fact that electrical resistance can be calculated from Ohm's law, since the current and voltage lines overlap (Shen, Li, Liaw, Delale, & Chung, 2007). The resistance method involves the application of two electrical contacts to send current and any number of electrical contacts to measure voltage in which the applied current line and the electric potential line coincide. In this research both narrow and wide specimens have been used as narrow specimens obtain large resistance values, since the resistance of a composite decreases with width (S. K. Wang et al., 2006). As a pair of electrodes is usually involved in the resistance measurement when using the two-probe method, contact resistance may occur due to imperfect bonding between the electrodes and the composite laminate. Thus, the four-probe method was proposed in which a pair of electrodes is used for the current input, while another pair of electrodes for the voltage output (Sevkat, 2008).

Resistance measurements as a non-destructive damage detection in carbon fiber composites were first used by Todoroki and Kobayashi (1994) in which they used the potential method for a real time non-destructive evaluation method of delamination of unidirectional stacked carbon fiber reinforced polymer composite. They pioneered using

electric resistance to detect delamination by initiating Mode I and Mode II delamination tests. Delamination crack length was measured with reading microscopes. They attached electrodes by sanding the surfaces, painted conductive silver paint, and attached an electrode and strain gauge terminals to the surface aligned with a perpendicular line to the crack growth direction (Todoroki and Kobayashi 1994).

Their experiments show that the electric resistance increases almost linearly with delamination crack growth even in the mode II test in which the delamination crack surfaces keep contact with each other. Provided that the delaminating crack of mode II propagates unstably under the condition of a $L < 0.7$, the impact causes relatively large electric resistance change of electrodes and the delamination crack could not be detected. Thus, it is thus very important in cases of small resistance change. It was concluded that the bridge method needs low current to give precise measurements (Todoroki and Kobayashi 1994).

Other methods in exploiting the electrical conductivity of carbon fiber samples see the same results where resistance change is correlated with damage. It is important to note ways in which damage through changes in resistance is detected.

CFRP composite samples see conductivity that is not isotropic and depends on the orientation and on the conductivity of the carbon fibers. Changes in the conductivity can therefore be related to fiber fracture (Shultz and Baron, 1989). In CFRPs the conductivity depends on the direction and the orientation of the conducting fibers; so there exist large differences between conductivity in the longitudinal and the transverse fiber directions. In the transverse direction, the resistance is generally higher because of the (usually, non-conducting) matrix whereas in the longitudinal direction, because of the continuous fiber path, there is lower resistivity.

Prior to fiber fracture, the conducting path should be essentially along the fiber direction, and the resistivity should be low. As damage accumulates during fatigue and individual fibers break, in order to complete the conducting path there necessarily must

be some current flow in the transverse direction, accompanied by an increase in resistivity (Weber and Schwartz, 2001). In sensing damage in textile fibers, if there is no damage and/or percolation, the change of resistance is linearly proportional to strain due to piezoresistivity of the conductive fibers. Then, due to the excessive damage of the fibers and/or large straining, the resistance change can increase dramatically with increase of the strain. It has been observed that the relation between the resistance change and tensile strain follows an exponential or power law (Sevkat et all, 2008).

However, what is limiting in woven textile composites is in the perspective of the experimental local strain analysis, due to the heterogeneity of textile composites, classical electrical resistance strain gauges do not have adequate spatial resolution and only a full-field strain measuring technique with high spatial resolution and strain sensitivity can be applied to determine local surface strain profiles (Daggumati and Voet, 2011)

What was limited in all of the preceding research was the ability to do simultaneous data collection of impact and load along with change in resistance particularly in the area of carbon fiber textile composites. Many of the previous research dealt with unidirectional carbon fiber composites that did not involve weaved carbon fiber textile composites. Thus, this thesis seeks to improve upon previous methods as well as modify experimental setups and extract new data on the electrical resistance and impact damage in textile composite.

1.4 Thesis objectives

The objective of this thesis was threefold and includes the ability to develop a fully-automated experimental setup that allows for highly accurate real time measurements of the electrical resistance in textile composites subjected to low velocity impact; to determine electrical resistance of 5-harness satin carbon fiber polymer matrix textile composites; and to determine the effectiveness of the one dimensional electrical

resistance method at sensing damage in 5-harness satin carbon fiber polymer matrix textile composites subjected to single and repeated low velocity impacts. This thesis is separated into multiple sections, the first of which are background information and literature review that are then followed by the thesis objectives. The techniques used in identifying the textile in addition to specimen preparation are discussed in Chapter 2. The equipment used and the results in the four-probe resistance measurement experiments are discussed in Chapter 3. The experimental results obtained from simultaneous low-velocity impact tests and its correlation with resistance changes are reported in Chapter 4. A summary of all work and recommendations for future work are given in Chapter 5.

CHAPTER 2
MATERIALS AND SPECIMEN PREPARATION

2.1 Sample Identification

The samples used in this thesis are 5 Harness Satin symmetric textile laminates with a 45 degree warp direction in top and bottom layers as seen in Figure 2.1.

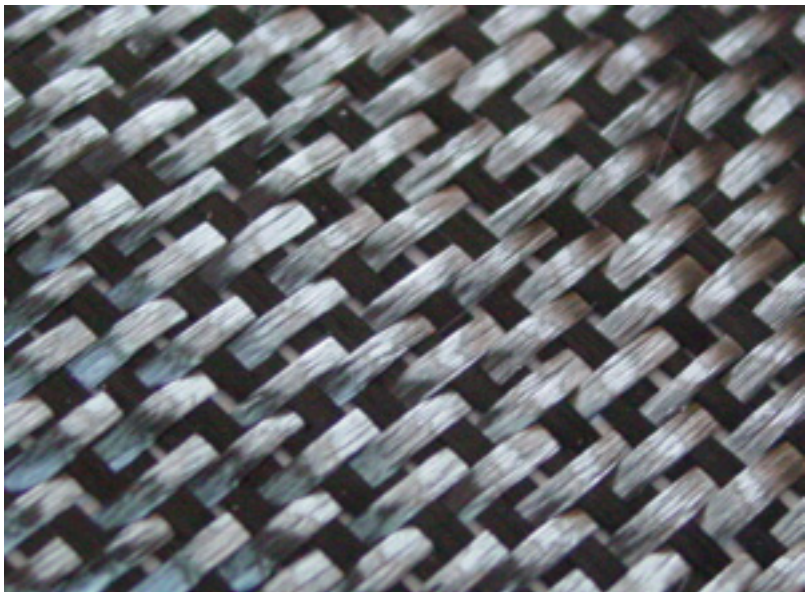

Figure 2.1: Harness Satin Weave with 45-Degree Orientation (Composite Envisions, 2012)

According to the Hexcel Aerospace Selector Guide, the weave and orientation were determined to be that of CF 5 Harness Satin 4 by 1 with an orientation of 45 degrees (Hexcel, 2010).

2.2 Sample Dimensions

The samples came from two large panels. The following Figure 2.2 and Figure 2.3 show the dimension of cutting for original composite plate samples. Accordingly, Figure 2.4 shows the small specimen after cutting into pieces with the mark on them.

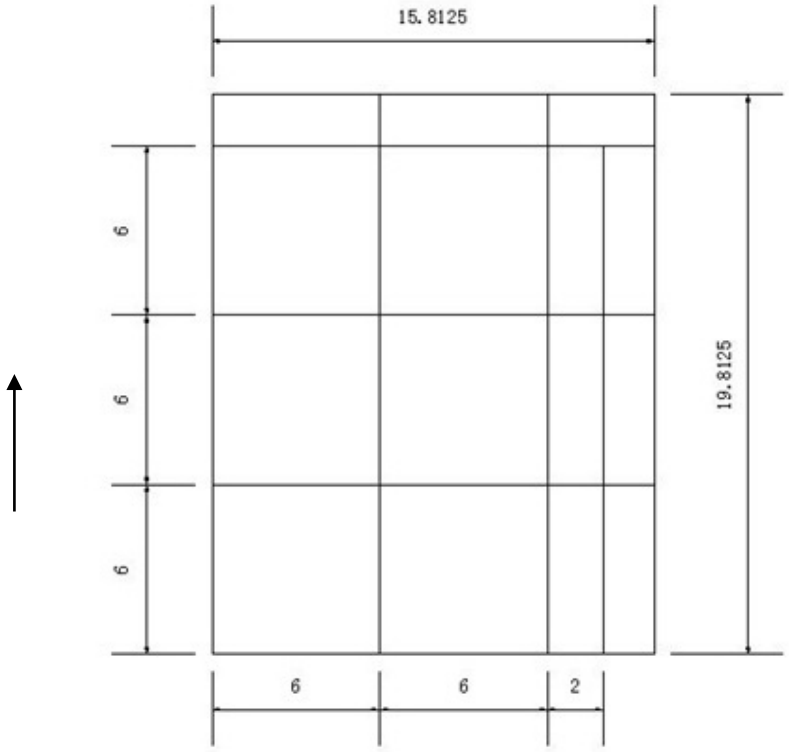

Figure 2.2: Original Composite Plate 1 as well as Cut Lines Required (Black Arrow Indicates the 0^{o} Direction) (Song, 2013)

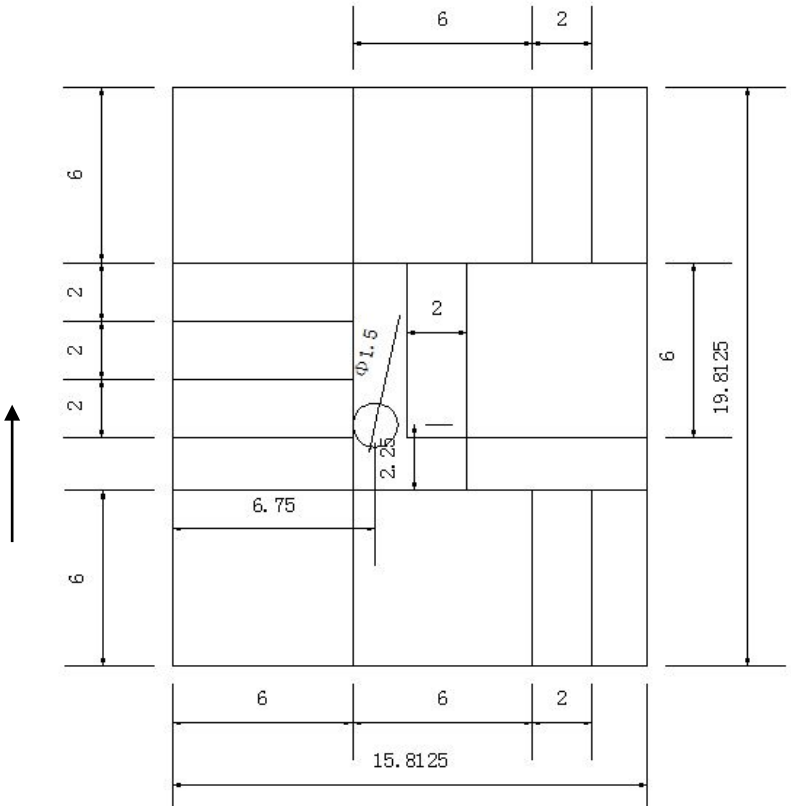

Figure 2.3. Original Composite Panel 2 as well as Cut Lines Required (Black Arrow Indicates the 0^{o} Direction) (Song, 2013)

To track the samples a two number identification system was used. The first number represents the panel, from which the sample was cut, and the second contained the sample number. An identification number and an arrow indicating the fiber direction were written on each sample. The samples were cut into horizontal beams and square plates with the use of a water jet. The water jet is chosen for its ability to produce finished edges (Hill, 2012); however, due to poor gripping of the panels upon cutting, some of the samples had rough and uncut edges with some delamination. The condition of each sample from both panel 1 and panel 2 is summarized in Table 1 and seen in Figure 2.4

Table 2.1: Conditions of Samples from Panel 1 & Panel 2

Square Samples		Beams	
1-1	Smooth Edges	1-7	Cuts into the laminate top right corner
1-2	Smooth Edges	1-8	Smooth but unevenly cut
1-3	Smooth Edges	1-9	Jagged cut into the laminate
1-4	Cut to be higher than samples 1-3. Small divet in right hand side	2-6	Left corner delamination. Right bottom corner, jagged cut
1-5	Poorly cut smaller than and even than samples 1-3	2-7	Delamination upper left corner
1-6	Completely uneven and poorly cut	2-8	Smooth Edges
2-1	Smooth Edges	2-9	Smooth Edges
2-2	Smooth Edges	2-10	Smooth Edges

Figure 2.4: Delamination in One of the Samples

Beam samples 1-7 through 1-9 and 2-7 through 2-9 were used for the electrical characterization, as those samples featured less damage and little to no delamination, which may affect their electrical characterization.

There were 6 square plates and 3 horizontal beams cut from panel 1 and 5 square plates and 5 horizontal beams cut from panel 2. In order to properly measure and categorize each sample, measurements of each corner starting at the right hand corner turning the sample clockwise were taken. The length was taken as parallel to the fibers, the width was taken perpendicular to the fiber orientation, and the four thicknesses were taken at each of the corners. The dimensions of each sample are seen in Table 2.2 and 2.3.

Table 2.2: Dimensions of Square Samples

Square Samples	Width (Perpendicular) [mm]	Length (Parallel) [mm]	Thickness [mm]
1-1	147.565	152.23	4.5
1-2	152.67	151.39	4.52
1-3	152.715	152.545	4.54
1-4	150.75	152.105	4.57
1-5	149.95	150.83	4.61
1-6	147.9	156.915	4.59
2-1	147.565	153.475	4.58
2-2	153.215	153.34	4.54

Table 2.3: Dimensions of Beam Samples

Beams	Width (Perpendicular) [mm]	Length (Parallel) [mm]	Thickness [mm]
1-7	149.1	51.23	4.49
1-8	148.69	48.95	4.58
1-9	151.72	45.85	4.45
2-6	153.12	51.47	4.5
2-7	153.4	51.55	4.58
2-8	153.47	51.61	4.64
2-9	153.4	51.89	4.63
2-10	153.43	51.75	4.56

2.3 Composite Sample Preparation

2.3.1 Composite Sample Preparation

The composite samples were prepared for electrical characterization using the method utilized by Hill (2012). First, spacing of the wires was determined in order to have efficient placement of the probes on the sample. It was decided that a spacing of 1 1/8 of an inch for each probe on the top and bottom surface would be more efficient. A

wooden block with 600 grit sandpaper was used to sand down the lines drawn indicating the probe spacing as seen in Figure 2.5.

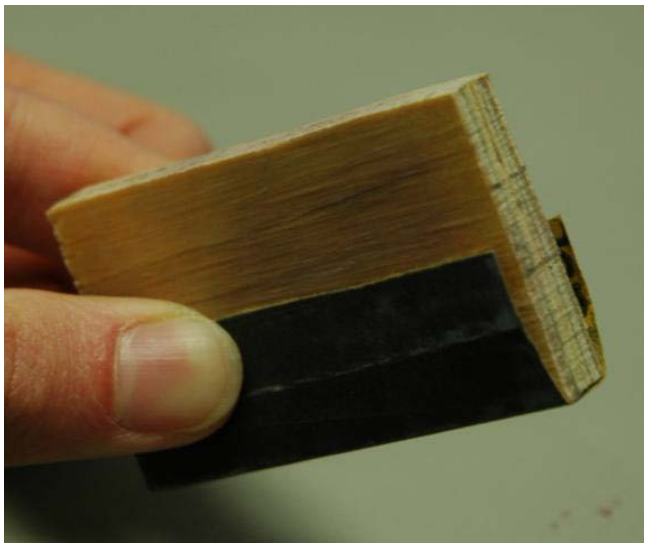

Figure 2.5: Wooden Block with 600 Grit Sandpaper (McAndrew, 2009)

Acetone was then used to clean the residue away. The width of each space was about a quarter inch and was cordoned off with tape in which silver paint would be applied. The silver paint would better allow for conductivity through the probe and composite.

2.3.2 Probe Preparation

Conductive wire was used for the probes. A spool of wire was cut above the desired length of about four inches, with blue masking tape lined to the exact measurement. Once cut, the wire was placed in a vice and pulled until straight with pliers. 24 wires were made for the composites. Once all were straightened, the wires were taken

back the samples in which a thin coat of silver paint was applied to the sample. While still wet, the wires were placed on the paint and placed so that they would hang over one side of the sample for electrode attachment. Sometimes, the wooden block was used to nudge the wires into the correct position as seen in figure. Once placed, another layer of silver paint was painted over the probe for further adhesion. This was repeated for the remaining samples.

Once all were dried, a layer of conductive epoxy was applied over the already attached electrodes. The epoxy was spread across the probes on the sample. All samples were left to dry for 24 hours to ensure the epoxy was fully cured. The last step in the sample preparation procedure was to smooth the cured epoxy surfaces to remove any excessive material and again minimize any contact resistances that could occur between the samples and electrodes (Hill, 2012). The epoxy used is seen in Figure 2.6

Figure 2.6: Epoxy Applicator (McAndrew, 2009)

Figure 2.7 shows the finished and prepared sample.

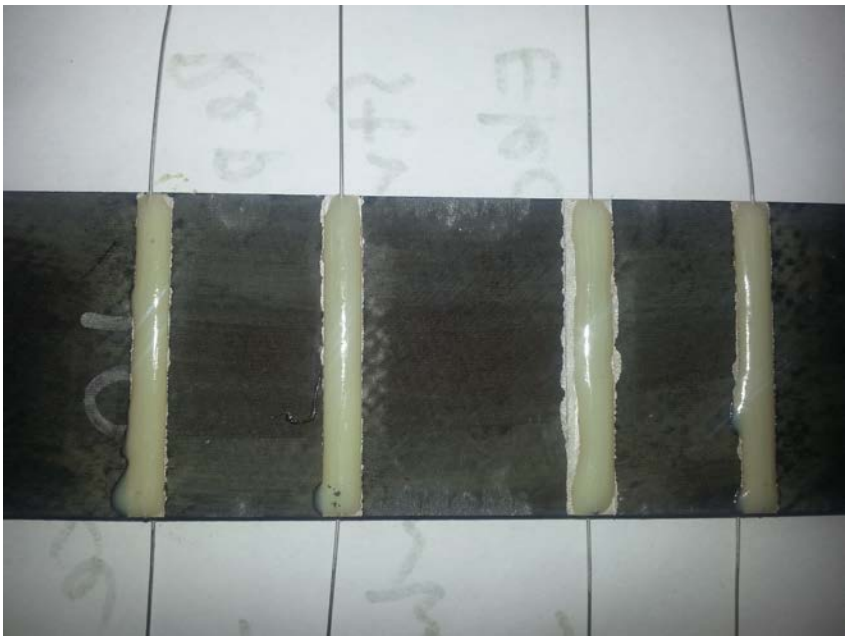

Figure 2.7: Prepared Sample

Electrical characterization testing could now begin.

CHAPTER 3
FOUR PROBE ELECTRICAL CHARACTERIZATION TESTS

3.1 Experimental Considerations

The purpose of the electrical characterization tests is to get baseline resistance measurements of the textile composite beam samples. When doing non-destructive damage sensing, getting an initial resistance to compare to the resistance taken during and after impact is important. While this thesis uses similar experimental setups as those in (McAndrew, 2009; Hill, 2012), the composite being tested is different than composites used in previous research. One of the objectives of this work is to determine if the experimental setup developed in the previous studies for testing composites with straight continuous carbon fibers and carbon nanotube buckypapers provide accurate measurements of the electrical resistance in textile composites. Another objective was to develop an experimental setup that enables real time measurements of the electrical resistance during low velocity impact testing, as it was not achieved in the previous work.

3.2 Hill's Experimental Setup

This section describes an experimental setup developed by Hill (2012). The experimental setup for electrical characterization primarily consists of Agilent U2531A DAQ and the HP 6612C Power supply all connected to a computer with VeePro software that records the resistance through the composite sample. The scheme of this experimental setup is shown in in Figure 3.1.

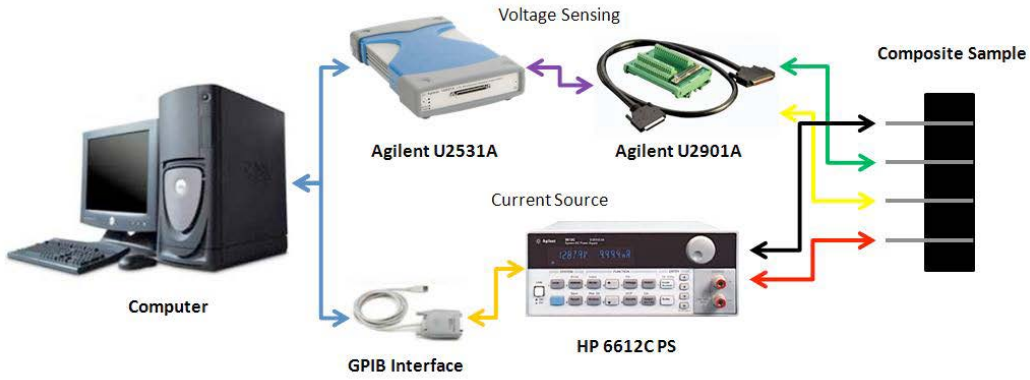

Figure 3.1: Hill's Experimental Setup (Hill, 2012)

3.2.1 Hardware

The setup developed by Hill (2012) uses a HP power supply in order to supply current and a U2531A DAQ system to sense voltage and then the resistances of the composite on its top, bottom, and oblique surfaces are computed. To supply constant source direct current and power to the four electrical probes, an Agilent 6612C Power Supply is used as well as an Agilent 6612C Power Supply to determine voltage.

Agilent's VEE Pro version 8.5 software is used as DAQ software to determine the voltage sensed by the U2531A DAQ and the program was written by Hill (Hill, 2012). The voltage and current are recorded and the power supply current and voltage sensed by the DAQ are used to determine the baseline resistance through the top, bottom, and oblique surfaces of the samples.

3.3 Four Probe Experimental Procedure

In this research four probe electrical resistance measurements have been performed on six textile composite samples, three from the panel 1 and three from panel 2. Electrical characterization tests were performed on top, oblique and bottom surfaces at

currents of 10, 30, 50, 70, 90 and 110 mA. Ten resistance measurements were performed at all current levels on each sample. The Agilent U2531A data acquisition unit was used as it has a maximum sampling rate of two million samples per second.

3.3.1 Experimental Procedure

First, the data acquisition software VeePro was opened using the New DC program file that was previously modified by Hill (2012). The electrodes were then attached to the probes located on the surface for testing. To perform top surface electrical characterization, the electrodes measuring the voltage from the DAQ were placed on the two probes on the inside of the sample ¼" away from the composite edge. The electrode measuring the current from the positive output of the HP6612C Power Supply was placed on the outermost probe while the electrode from the negative output was placed on the opposite side. The configuration of the setup is seen in Figure 3.2.

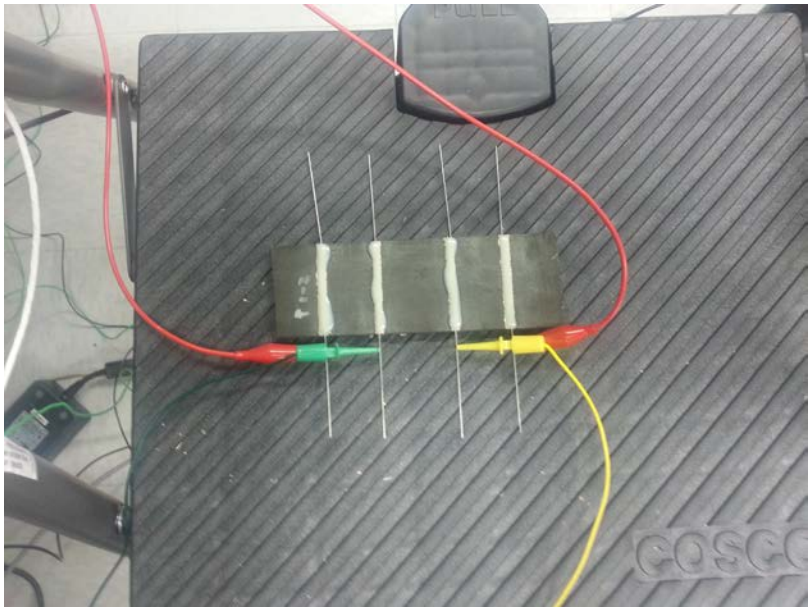

Figure 3.2: Probe Placement for Resistance Measurements

To perform bottom surface characterization, the sample was flipped over and the same convention was used as in the top.

Currents of 10, 30, 50, 70, 90 and 110 mA were set and ten resistance measurements were performed at the current levels on each sample. The power supply voltage did not exceed 1-2V.

Time was initially not available to complete the oblique surface, but the procedure was completed using Hill's method such that the positive terminal of the power supply was connected to one of the outermost electrodes on the top surface of the samples. Then the power supply's negative output was connected to outermost electrode on the bottom surface of the composite on the opposite side of the sample from the connection on the top surface. The DAQ connections were done in a similar manner with the terminals being connected to the innermost electrode on the top and bottom surfaces of the sample on the same sides as the power supply connections (Hill, 2012).

3.4 Top and Bottom Results for Initial Experiments using Hill's Setup

The top and bottom experiments were performed on May 6th, 2013. The final resistances of the bottom and top surfaces of samples 1-7, 1-8, 1-9 are seen in Figures 3.3 and 3.4.

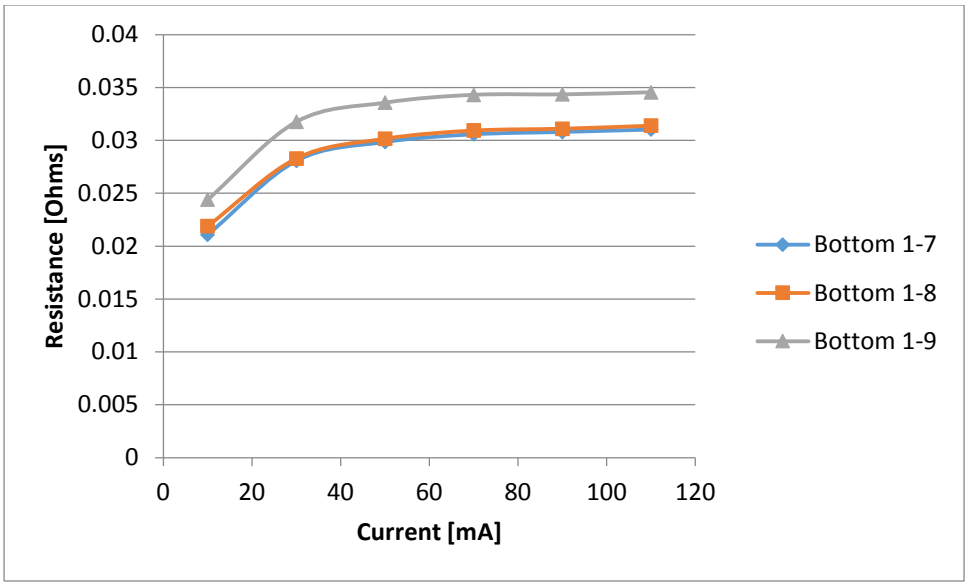

Figure 3.3: Bottom Surface Resistances for Panel 1 Samples

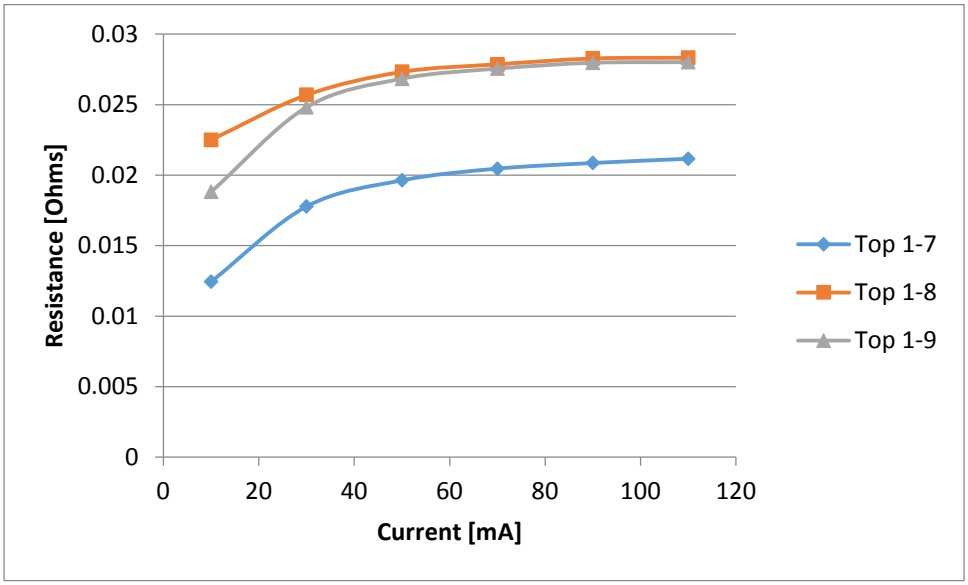

Figure 3.4: Top surface resistances for panel 1 samples

The data shows the average resistance at each current for each sample from panel 1. There was no variation in voltage and it did not exceed 1-2 V. Within each surface, the

resistance increased with increasing current yet increased at a constant rate. However, when the resistances are compared between each sample and surface, the composite exhibits a higher resistance in the bottom surface than in the top surface with sample 1-9 having the larger resistance amongst the three samples.

The results for panel 2 bottom and top resistances for samples 2-7, 2-8, and 2-9 are seen in Figures 3.5 and 3.6.

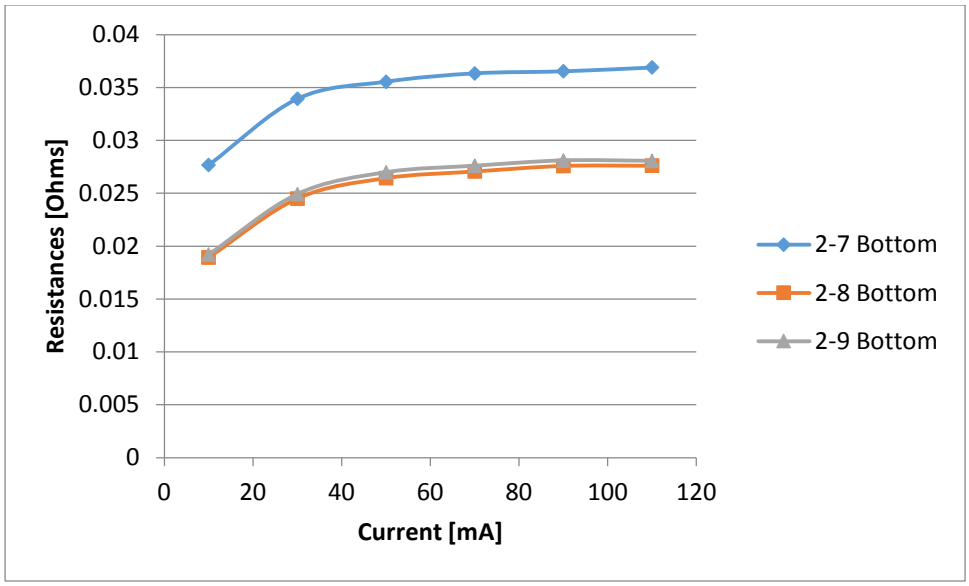

Figure 3.5: Bottom Surface Resistances for Panel 2 Samples

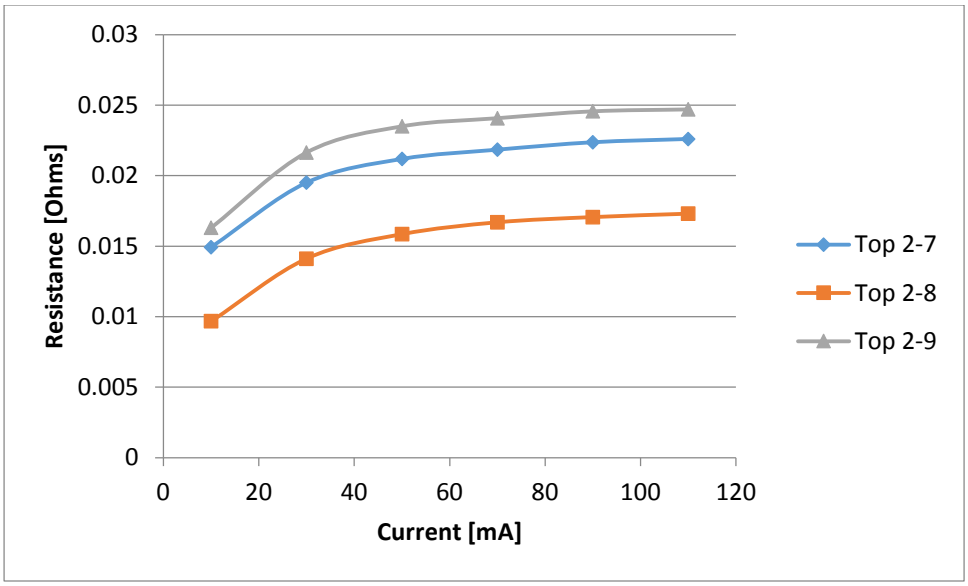

Figure 3.6: Top Surface Resistances for Panel 2 Samples

Again, the data shows the average resistance at each current for each sample from panel 2 with resistance steadily increasing with increasing current. As one can see, there is resistance variability when compared between samples and surfaces, with sample 2-7's bottom surface posting higher levels of resistance than the other samples.

3.5 Second Set of Bottom Electrical Resistance Experiments using Hill's Setup

The experiments were resumed in August 2013. Before new testing could begin, retrials of sample 1-8 bottom surface were performed to confirm the results obtained earlier and reported in the previous section. The error analysis was also performed to determine the accuracy of the measurements, which is described further in Section 3.6. The percent error for each current level on sample 1-8 is seen in Table 3.1 and the graph documenting the old and new resistances vs. current is seen in Figure 3.7.

Table 3.1: Percent Errors of Sample 1-8

Current [mA]	Percent Error [%]
10	0.116
30	0.0712
50	0.0567
70	0.0579
90	0.049
110	0.0503

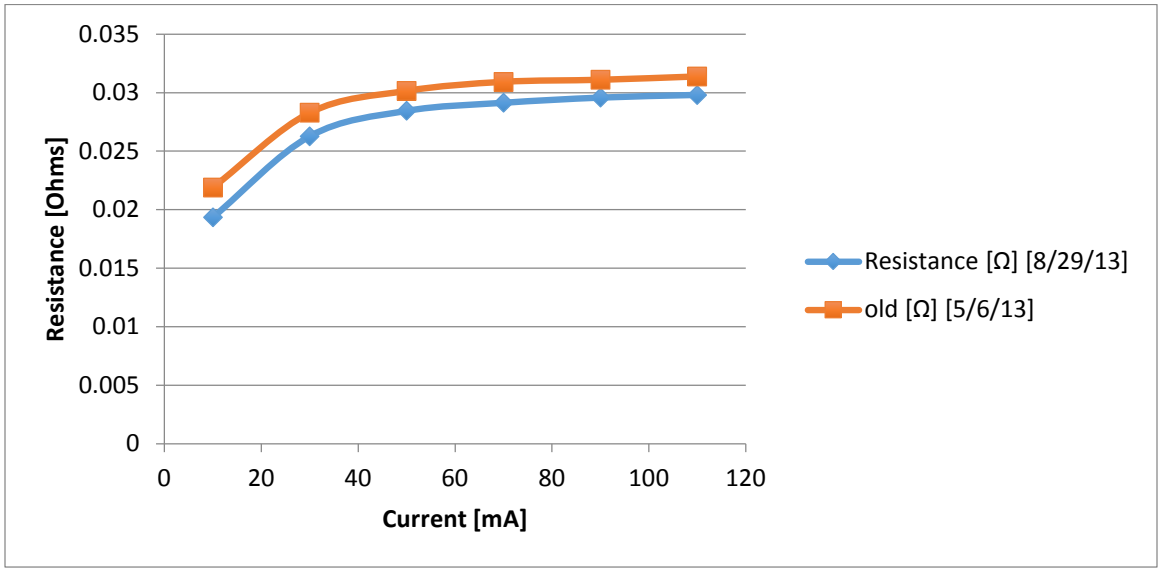

Figure 3.7: Sample 1-8 Bottom Resistance vs. Current Comparison between Measurements

As seen in the results, the percent error does not deviate wildly, especially with increasing current and further experiments at the lower current were completed.

3.6 Error Analysis for Hill's Setup

In this section the error analysis for the measurements conducted using Hill's setup (Hill, 2012) is presented. Using the U2531A DAQ and Power Supply 6612C, the elemental errors of the equipment were found using the elemental uncertainty analysis previously conducted by Hill (Hill, 2011). Table 3.2 shows DAQ and power supply elemental uncertainties.

Table 3.2: Elemental Uncertainties in U2531A DAQ and Power Supply 6612C (Hill, 2011)

DAQ Uncertainty	[V]	**DC Power Supply**	[A]
Resolution	1.90735E-05	Resolution	0.001
ε_o	0.002		
ε_g	0.006		
u_o^{DAQ}	9.53674E-06	u_o^{PS}	0.0005
u_e^{DAQ}	0.006324555	u_o^{PS}	0.0000025
u_d^{DAQ}	**0.006324563**	u_d^{PS}	**0.000500006**

The following notations are used in Table 3.2: u_o is standard uncertainty or half the resolution, u_e is elemental uncertainty that is the sum square root of the offset error, ε_o, and gain error, ε_g; u_d^{DAQ} and u_d^{PS} are sum square root of the standard and elemental uncertainties in DAQ and power supply, respectively.

Three errors were calculated using Hill's method. The accuracy of the DAQ, ε^{DAQ}, was calculated by taking the average voltage measurement of the DAQ, V^{DAQ}, and the offset error, ε_o, and gain error, ε_g:

$$\varepsilon^{DAQ} = V^{DAQ} - \left(V^{DAQ} - \varepsilon_o\right)\frac{1.25}{1.25+\varepsilon_g} \tag{3.1}$$

The total uncertainty of the DAQ, ε_{total}, is calculated as Equation (3.2) takes into account the accuracy of the DAQ that was just calculated in equation (3.1) and the standard uncertainty of the DAQ:

$$\varepsilon_{total} = \sqrt{\left(u_o^{DAQ}\right)^2 + \left(\varepsilon^{DAQ}\right)^2}. \tag{3.2}$$

Finally, the error propagation between the power supply and the DAQ, U_{sys}, is calculated as

$$U_{sys} = \sqrt{\left(\frac{\varepsilon_{total}}{I^{PS}}\right)^2 + \left(u_d^{PS}\frac{V^{DAQ}}{(I^{PS})^2}\right)^2}, \tag{3.3}$$

where I^{PS} is the average current of the power supply.

The total uncertainty in the resistance for the bottom surface sample 1-8 using the second set of data on Sample 1-8 reported in Section 3.5 is seen in Table 3.3.

Table 3.3: Bottom Resistance Measurements
with Total Uncertainty Errors Sample 1-8

Current [mA]	Resistance [Ω] [8/29/13]
10	0.0193± 0.201
30	0.0263± 0.0616
50	0.0284± 0.0400
70	0.0291 ± 0.0287
90	0.0296± 0.0222
110	0.0298± 0.0181

From the results it is determined that the uncertainty error decreases with increasing current. This has precedent as discussed in Hill's previous research, he remarked on how one of the issues with using his experimental setup was that while the sampling rate is very fast, the noise produced from the DAQ is large due to the low voltage being measured (Hill, 2011). Thus, higher currents should produce better data with lower error and noise than that at lower currents.

3.7 McAndrew's Experimental Setup

The initial problems faced by using Hill's setup were that there was some indication that the accuracy of the electrical resistance measurements may not be acceptable for damage detection in textile composites. Thus, the experimental setup developed by McAndrew (McAndrew, 2009) was used. The previous studies found that McAndrew's setup can provide accurate low electrical resistance measurements, but at the same time does not allow real time resistance measurements during the low velocity impact tests. The limitation came from the low sampling rate. It is worthy to note that development of the Hill's setup was motivated by this limitation, but came at a price of the measurement accuracy.

3.7.1 Hardware

McAndrew's setup involves a nanovolt/micro ohmmeter, an input cable for the micro ohmmeter, a data acquisition (DAQ)/switch unit, a multiplexer (MUX) card, two GPIB cords, a GPIB to USB cord, electrical leads, and a computer. The nanovolt/micro ohmmeter is an Agilent model number 34420A and is used to make four-wire resistance measurements (McAndrew, 2009). It measures the switch unit on the multiplexer cards. Since the 34420A only has two measurement channels (four less than that needed), a data acquisition/switch unit with a multiplexer card was required (McAndrew, 2009).

The 34907A DAQ was used as a switch unit to open and close the channels to be measured by the 34420A. Supplying the channels was an Agilent 34901A multiplexer card that contains source and sense channels capable of supplying and sensing the four wire-resistance method of the sample.

To make 4-wire resistance measurements at the input terminals of the micro ohmmeter, a special input cable is attached to a pair of Kelvin clips, which is connected

to the sample. However only a single 4-wire resistance measurement can be performed using this method. Since it was desired to make three 4-wire resistance measurements (top surface, bottom surface, oblique), the input cable was instead connected to the common terminals of the multiplexer card (McAndrew, 2009).

Six channels, each containing a high and low lead, were used to make the three desired 4-wire resistance measurements. To make a 4-wire resistance measurement using the 34901A multiplexer, an n-source channel is paired with an n+1 sense channel (Agilent Technologies, 2006). For the top surface resistance measurement, channel 8 was selected as the source, or current, channel. Thus channel 18 was required to be the sense, or voltage, channel for the top surface resistance measurement. Similarly, channels 9 and 19 were used for the bottom surface resistance source and sense channels. Finally, channels 10 and 20 were used for the oblique resistance source and sense channels. After stripping off the ends of all leads and installing them in the correct channel terminals, the multiplexer was inserted into the first slot of the data acquisition/switch unit (McAndrew, 2009). The base number of this scheme (100, 200, or 300) refers to which slot the plug-in module is in (the first, second, or third). The last two digits represent the module channel number (Agilent Technologies, 2006). These channels are seen in Table 3.4.

Table 3.4: Channel and Surface Connections

Resistance Type	Channel Number	Function
Top Surface	108	Source (current)
	118	Sense (Voltage)
Bottom Surface	109	Source (current)
	119	Sense (Voltage)
Oblique	110	Source (current)
	120	Sense (Voltage)

A GPIB cord was connected to the computer and although initially connected to the power supply in McAndrew's initial setup, the GPIB cord was directly connected to the micro ohmmeter and DAQ. With this modification, three 4-Wire Resistance measurements could be made at a source current of 10 mA. The final setup of the hardware with the DAQ, Multiplexer and micro ohmmeter are seen in Figure 3.8.

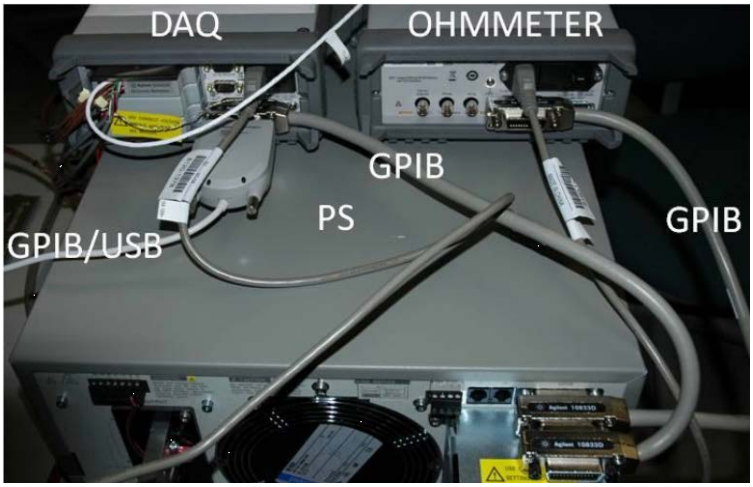

Figure 3.8: Hardware Connection of the Ohmmeter, DAQ, and Multiplexer (McAndrew, 2009)

3.8 McAndrew's Experimental Procedure

Using VeePro software programmed by McAndrew (2009), electrical characteristic testing was able to commence by attaching the high and low alligator clips to the probes to measure the top, bottom, and oblique surfaces. For the top surface, channel 108 and 118 Hi and Lo alligator clips were connected to the probes. For the bottom, channel 109 and 119 Hi and Lo alligator clips were connected to the probes. To measure the resistance through the oblique surface, channel 110 and 120 alligator clips

were also connected to the probes. The schematic or how the connections were made are seen in Figure 3.9. Resistance measurements were made on the six samples using a source current of 10 mA.

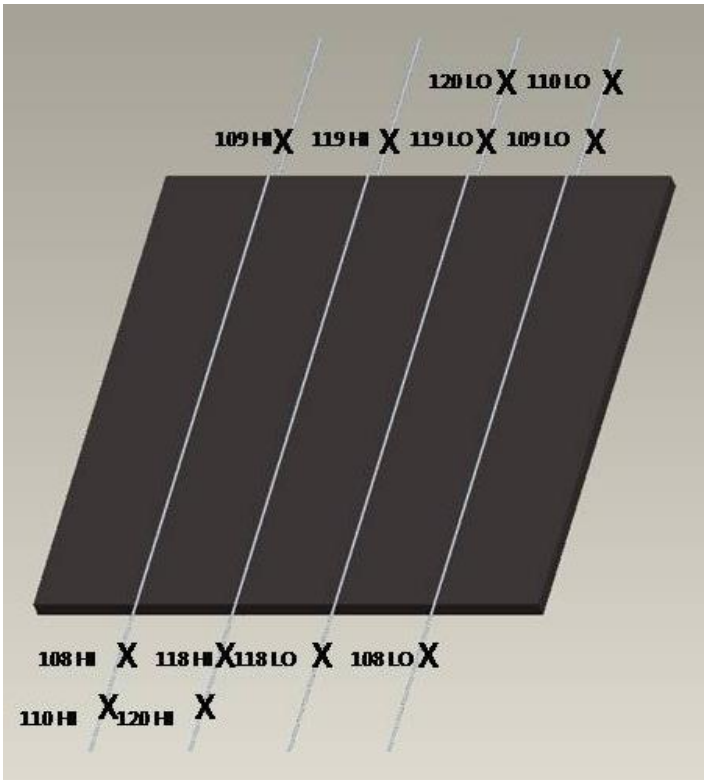

Figure 3.9: Electrical Lead Attachment (McAndrew, 2009)

3.9 Experimental Results Obtained using McAndrew's Setup

Using McAndrew's Setup, ten resistance measurements were taken from each surface on each of the six samples. The results were averaged and the recorded in Table 3.5.

Table 3.5: Resistance Measurements for Six Samples at Source Current of 10mA

	Bottom [Ω]	Top [Ω]	Oblique [Ω]
Sample 1-7	0.0202	0.0388	0.0556
Sample 1-8	0.0324	0.0314	0.0468
Sample 1-9	0.0302	0.0367	0.0611
Sample 2-7	0.0398	0.0229	0.0603
Sample 2-8	0.0306	0.0192	0.0452
Sample 2-9	0.0295	0.0258	0.0509

3.10 Error Analysis for McAndrew's Setup

In order to validate the results on the textile composites using McAndrew's setup, an error analysis was conducted as outlined in his thesis (McAndrew, 2009) and following the calculations in the report of Wang (Wang, 2012).

3.10.1 Calculating the Voltage Error in the Standard ε_{std}

In order to get an accurate error in the equipment and through the sample, several steps were used as outlined in McAndrew's thesis were completed (McAndrew, 2009). The 34420A ohmmeter was shorted at its terminals due to the fact that the 34420A is more accurate at its terminals. This was accomplished by taking out the four wires located in the multiplexer/switch unit that were connected to the source and sense channels. These wires were then tied together to create a short after which 10 resistance measurements were taken. In order to calculate the resistance error in the standard, equation (3.4) was used.

$$\varepsilon_{std} = \sqrt{\left(\varepsilon_{p,stdt}\right)^2 + \left(\varepsilon_{cal}^{DAQ}\right)^2}, \tag{3.4}$$

where ε_{std} is the resistance error in standard, ε_{cal}^{DAQ} is the calibration error of the micro ohmmeter, and $\varepsilon_{p,std}$ is the precision error in the 10 measurements that was obtained by shorting the ohmmeter at the terminals as defined by the following equation

$$\varepsilon_{p,std} = t_{v,p}\frac{s_x}{\sqrt{N}}, \tag{3.5}$$

where *t* is a value from the student-t distribution table, *N* is the number of measurements, *v* is the degrees of freedom (v =*N*-1), s_x is the sample standard deviation of the 10 measurements, and *P* is the probability level (p =95% was used in the experiment) (Figolia, Beasley, 2000). Four sets of data were taken giving errant results; thus, after 20 minutes the fourth set of measurements provided an error in the standard that was similar to that given by McAndrew's reported error. Thus, it is recommended to allow the machine to warm up for about 20 minutes to allow for more accurate results faster.

To find the calibration error of the ohm meter, ε_{cal}^{ohm}, the accuracy equation is seen in equation (3.6)

$$\varepsilon_{cal}^{ohm} = \frac{\sum_{i=1}^{10} 0.007R_i + 0.002 * range}{10}, \tag{3.6}$$

where R_i are resistance measurements. This formula is specified in the Agilent 34420A micro ohmmeter manual (Agilent, 2006). According to the student T-distribution table, $t_{10,0.95} = 1.833$. Therefore, the resistance error in the standard can be calculated using Equation (3.4).

3.10.2 Calculating the Calibration Voltage Error in the Measurement System ε_{cal}

Following McAndrew's thesis, each of the measurement systems (the micro ohmmeter and leads) that represent the resistance types (top, bottom, oblique) were calibrated (McAndrew, 2009). The sense and source wires were re-hooked to their terminals in the multiplexer for accurate readings of the resistances in the leads. The 4 alligator leads were shorted together and 10 readings were recorded for each surface using the calibration programs for each channel that represented each surface (channels 108, 109, and 110). Then, the precision error in the measurement system, the resolution bias error, and the bias error of the mean were calculated. The precision error was calculated by using equation (3.5). After that, the resolution bias error was calculated as:

$$\varepsilon_{res\_bias} = \frac{1}{2} resolution^{\,Agilent\ 34420A}, \tag{3.7}$$

where $resolution^{\,Agilent\ 34420A}$ was taken from Agilent user manual (Agilent, 2006).

The bias error of the mean of the measurements is the error of the measurements with respect to the calibrating standard. It can be calculated by

$$\varepsilon_{bias\_mean} = |x_{true} - x_{ave}|, \tag{3.8}$$

where x_{true} is the value of the standard (the average voltage value obtained during the shorting of the 34420A deck terminals), x_{ave} is the average of the 10 measurements during the shorting of the alligator leads of each surface.

Finally, the calibration error in the measurement system for one of the resistance types was calculated by taking the square root of the sum of the squares of the each of the calculated errors:

$$\varepsilon_{cal} = \sqrt{\varepsilon_{syst}{}^2 + \varepsilon_{res\_bias}{}^2 + \varepsilon_{bias\_mean}{}^2 + \varepsilon_{std}{}^2}\,, \tag{3.9}$$

where ε_{std} is calculated in equation (3.4).

3.10.3 Determining Resistance Error in the Sample

In the last step, the error in the resistance measurements of the sample were obtained by taking the original resistance measurements and finding the standard deviation of the original resistance measurements in the plate (or sample), or $\varepsilon_{p,plate}$. Thus the total resistance error in the plate is given by equation

$$\varepsilon_{plate} = \sqrt{\varepsilon_{p,plate}{}^2 + \varepsilon_{cal}{}^2} \tag{3.10}$$

3.11 Summary of Error Analysis of McAndrew's Setup

The accuracy that was achieved using McAndrew's setup and the aforementioned error analysis is ± 0.002 Ω on the top surface of sample 1-8 using a source current of 10 mA. These results were compared to McAndrew's accuracy of sample 7-16 in order to make sure the numbers achieved were reasonable (McAndrew, 2009). While McAndrew achieved an accuracy of ± 0.013 mΩ the resistance error on the top surface of sample 1-8 surfaces is much higher and is measured in Ohms. The comparison between McAndrew's resistance reported in his thesis and the textile composite of sample 1-8 resistance obtained in this study is shown in the Table 3.6.

Table 3.6: Comparison of Error in Resistance
in McAndrew and Sample 1-8

McAndrew Top Surface Resistance Sample 7-16 [mΩ]	Top Surface Resistance Sample 1-8 [Ω]
8.343±0.013	.0314 ± 0.002

The difference may be accounted for by the way the current enters the textile fibers than that of the composite McAndrew was using. Nevertheless, low resistance errors with respect to the measured resistance in sample 1-8 show that McAndrew's setup is more accurate.

Table 3.7 shows the total error in all of the measurements and samples this time in Ohms at a constant source current of 10 mA.

Table 3.7: Total Uncertainty Analysis for Beam Resistance Samples
at 10 mA using McAndrew's Setup

Sample	Bottom [Ω]	Top [Ω]	Oblique [Ω]
Sample 1-7	0.0201 ±0.00468	.0388 ± .000214	.0555 ± .000235
Sample 1-8	.0324 ±0.004688 Ω	.0314 ± .000204	.0467 ± .000233 Ω
Sample 1-9	.0303±0.00468	.0367± .000209	.0611± .000237
Sample 2-7	.0397±0.00468	.0229± .000204	.0602 ± .000235
Sample 2-8	.0306±0.00468	.0191± .000205	.0455± .0002338
Sample 2-9	.0295± 0.00468	.0258± .000201	.0509± .000233

3.12 Summary of Error Analysis of both McAndrew and Hill Setups

Table 3.8 shows resistance error comparison for Hill and McAndrew's setup using sample 1-8 through the bottom resistance.

Table 3.8: Sample 1-8 Bottom Surface Resistance Error Comparison between Setups

	Current [mA]	Resistance [Ω]
Hill's Setup	10	0.019± 0.201
McAndrew's Setup	10	0.0314 ± 0.002

It was determined from the above analysis that each of the setups had its own strength and weakness. Hill's setup is relatively fast and enables to perform real time electrical resistance measurement during low velocity impact tests. At the same time, resistance measurements in textile composites lack accuracy at low electric current (~10mA), when measurements are taken using Hill's setup. The errors produced by McAndrew's setup are low, but this setup is too slow and could not produce a single resistance measurement during the impact. Based on this analysis, it was decided to explore if the desired measurement accuracy using Hill's setup can be achieved at the higher electric current levels.

3.13 Performing Electrical Characterization Tests at Higher Currents

Resetting up Hill's setup, measurements of the top surface of sample 2-9 were completed to determine what higher source current would actually produce an error less

than 10%. Ten measurements were taken at various increments although the results for source currents from 490 to 750 mA were used to see if higher source currents would lower the uncertainty in Hill's setup. The results are seen in Table 3.9.

Table 3.9: Resistance Errors of Sample 2-9 Top Surfaces with Higher Source Current

Source Current [mA]	Resistance [Ω]	Error [Ω]	Percentage Error [%]	Temperature at leads [F]	Temperature at the surface [F]
490	0.02562	0.00395	0.15429	72	74.6
510	0.02562	0.00379	0.14810	72	75.4
550	0.02560	0.00351	0.13693	74	77.5
610	0.02536	0.00325	0.12822	74	79
630	0.02540	0.00314	0.12381	74	81
650	0.02538	0.00304	0.11987	74	81
690	0.02556	0.00286	0.11177	75.1	84.5
710	0.02574	0.00277	0.10769	74.2	84.7
730	0.02560	0.00269	0.10512	78.6	87.8
750	0.02567	0.00262	0.10192	75.1	89.5

It was determined that at 750 mA the uncertainty drops to 0.00262 Ω with a percentage uncertainty of 10.2%. Thus, to achieve a percentage uncertainty of 10% or less, source current has to be 750 mA or greater.

Note that during these tests, the temperature at the surface of the composite specimen was measured to ensure that there was no significant electric current-induced heating produced. Temperatures were taken using the Craftsman High Temperature infrared thermometer and were measured at the leads as well as the middle of the epoxy and surface. The temperature did increase with increasing source current with the surface temperature reaching 89.5 F at the 750 mA electric current. Due to this, it was decided not to increases the electric current further and perform electrical resistance measurement in all textile specimens at 750 mA electric current. The next section presents the results.

3.14 Electrical Resistance for Textile Composite Specimens at Higher Electric Current

The results of the electrical resistance measurements in specimens of Panels 1 and 2 are presented in Tables 3.10 and 3.11, respectively.

Table 3.10: Panel 1 Resistance Errors with Higher Source Current of 750 mA

Sample	Resistance [Ω]	Error [Ω]	Percentage Error [%]
1-7 Top	0.0211	0.00264	0.1249
1-7 Bottom	0.0427	0.00251	0.0590
1-7 Oblique	0.0591	0.00242	0.0410
1-8 Top	0.0311	0.00258	0.0829
1-8 Bottom	0.0302	0.00259	0.0856
1-8 Oblique	0.0459	0.00250	0.0545
1-9 Top	0.0313	0.00258	0.0825
1-9 Bottom	0.0349	0.00256	0.0735
1-9 Oblique	0.0593	0.00242	0.0408

Table 3.11: Panel 2 Resistance Errors with Higher Source Current of 750 mA

Sample	Resistance [Ω]	Error [Ω]	Percentage Error [%]
2-7 Top	0.0224	0.002549	0.1138
2-7 Bottom	0.0390	0.002449	0.0628
2-7 Oblique	0.0603	0.002322	0.0385
2-8 Top	0.0192	0.002568	0.1338
2-8 Bottom	0.0294	0.002507	0.0853
2-8 Oblique	0.0445	0.002416	0.0543
2-9 Top	0.0257	0.002616	0.1019
2-9 Bottom	0.0304	0.002501	0.0824
2-9 Oblique	0.0515	0.002375	0.0461

As the results show, the top surfaces of the samples in both panels have high uncertainties of 10% or greater. However, the oblique surfaces post the smallest uncertainty, which correlates to the fact that higher resistances produce lower uncertainties. Thus an accurate electrical characterization can be achieved using a higher source current using Hill's setup.

3.15 Electrical Resistance for Wider Textile Composite Specimens at Higher Electric Current

In addition to the horizontal beams, electrical resistance testing was conducted on the wider square samples of 6" by 6". The samples are from Panel 1 and are samples 1-1 and 1-2. The same electrode preparation was done on the samples. Electrical resistance measurements were performed using Hill's setup at 750 mA as seen in Figure 3.10 and the results are seen in Table 3.12.

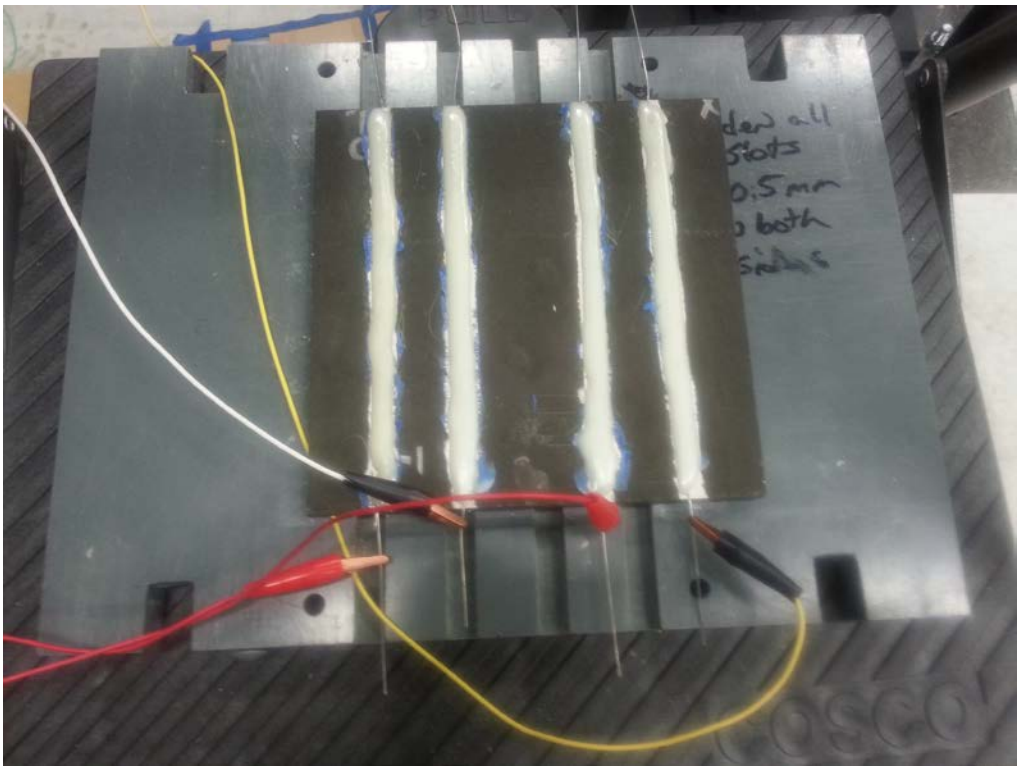

Figure 3.10: Electrical Resistance of Square Samples

Table 3.12: Electrical Resistance Errors
with Higher Source Current of 750 mA

Sample	Bottom [Ω]	Top [Ω]	Oblique [Ω]
Sample 1-1	0.01242 ± 0.000261	0.01318 ± 0.0000048	0.02079 ± 0.0000348
Sample 1-2	0.00961 ± 0.000029	0.01587 ± 0.000005	0.01767 ± 0.000014

The errors are low enough to show that a higher source current is more accurate on both square and beam samples using Hill's setup.

CHAPTER 4
IMPACT TESTS WITH ELECTRICAL RESISTANCE MEASUREMENTS

4.1 Motivation

One of the objectives of this thesis was to develop an experimental setup that enables real time measurements of the electrical resistance during low velocity impact testing, as it was not achieved in the previous work. A new setup developed in this work is based on Hill's setup (Hill, 2012) with modification enabling a simultaneous collection of the resistance measurements before and during impact. An ability to measure electrical resistance during the impact can be crucial for understanding how impact damage grows in the composite.

4.2 Modification for Simultaneous Resistance Measurements during Impact

4.2.1 Old Setup and Test Equipment

In Hill's previous setup (Hill, 2012), the Agilent 6612C power supply was used to trigger the pneumatic release that would release the drop weight. To coordinate resistance measurements and impact tests using both McAndrew's (McAndrew, 2009) and Hill's (Hill, 2012) previous impact setups, the HP 6692A Power Supply was also used.

Impact experimentation was performed using an Instron Dynatup Model 8200 Drop Weight Impact Testing Instrument, shown schematically in Figure 4.1.

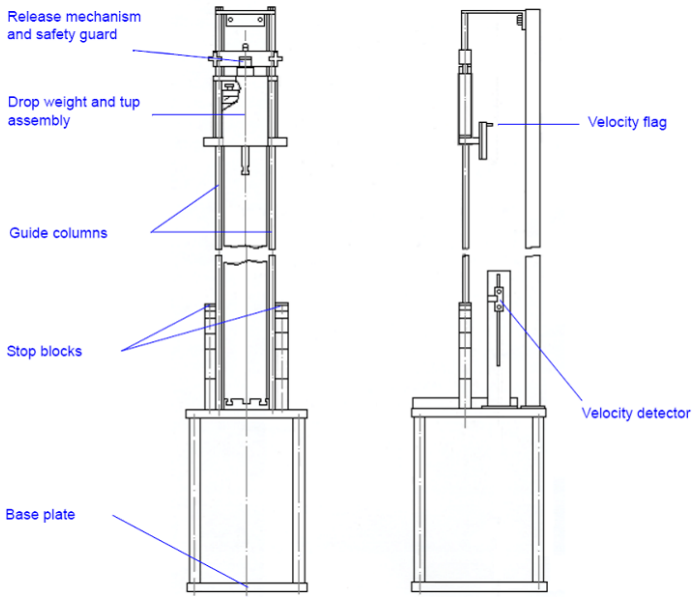

Figure 4.1: Schematic of the Instron Dynatup Model 8200 Drop Weight Impact Machine (McAndrew, 2009)

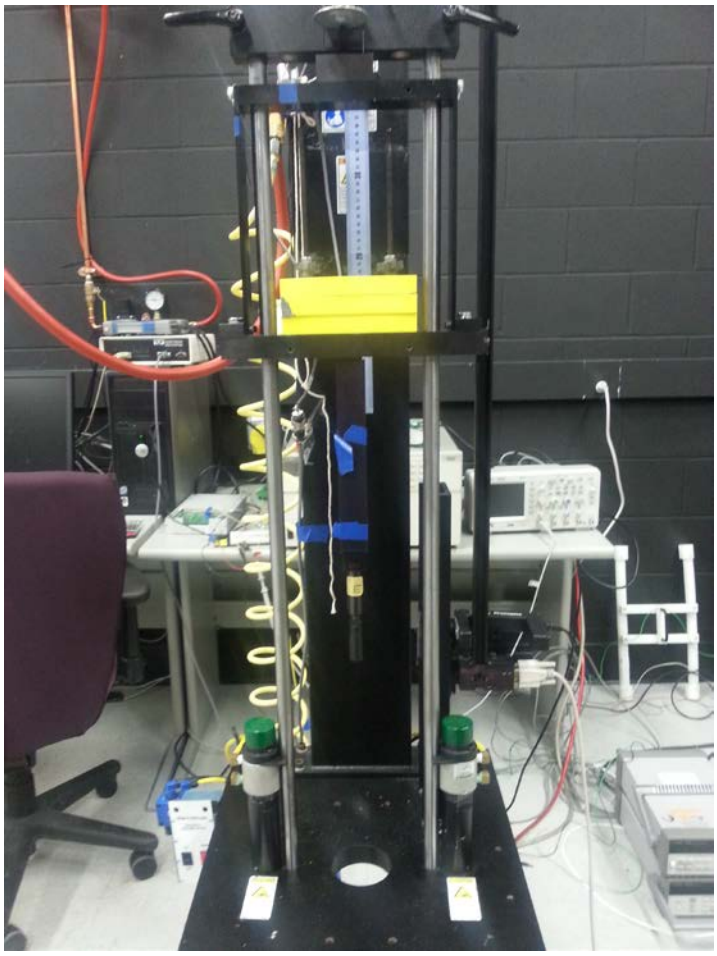

Figure 4.2: Impact Dynatup Model 8200

The impact tester is capable of producing impact energies ranging from 1.356 to 132.8 J (1.0 to 97.9 ft-lbs). The maximum impact velocity for the Instron Dynatup Model 8200 is 4.4 m/s (14.5 ft/s), while the maximum drop height is 1 m (3.28 ft) above the table (Instron Corporation, 2005).

The following is an overview of the Instron Dynatup Model 8200 operates. The drop weight assembly, which consists of the tup and tup insert, the velocity flag, and 1.67 kg blocks of mass, is raised until it connects to the clamp frame via the release lever. The desired height on the clamp frame is positioned with a ruler by loosening the two clamps on the clamp frame. This height determines the desired potential energy of the drop

weight assembly. The release mechanism is then depressed, allowing the drop weight assembly to fall freely. The velocity of the drop weight assembly is recorded using the velocity flag and the velocity detector, both shown schematically in Figure 4.3.

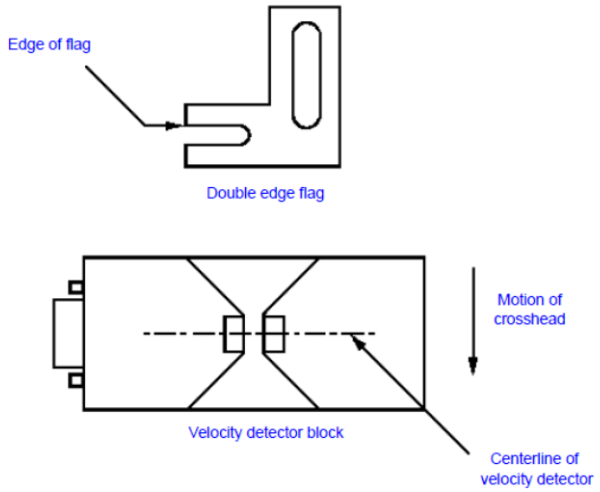

Figure 4.3: The Velocity Flag and Velocity Detector (McAndrew, 2009)

As shown in the figure above, the velocity flag has two metal prongs. When the top edge of the lower prong passes through the infrared light beam of the velocity detector on the photogate, the time is recorded. The time is also recorded when the bottom edge of the top prong passes through the velocity detector. Since the distance between the two prongs is known, the velocity can be calculated. Additionally, an Agilent OS01024A oscilloscope is also used in order to capture the flag's prongs pass the photogate. In Hill's previous pulse and impact setup, the oscilloscope was built into the current pulse generator and the settings on the oscilloscope were set to single sequence and the channels were adjusted using the control panel knobs to a point that the entire

pulse curve would be captured. The oscilloscope was not used as the main recording device for the experimentation but was relied upon as a backup in case the desktop computer failed to capture the pulse event (Hill, 2012).

In this work, modification to the Agilent Manager U2531A TW4903514 DAQ program is also completed in order to trigger the oscilloscope to collect resistance measurements. The Agilent Manager is a software program in which all controls are operated through a user interface rather than having to be programmed line by line such as in the VEE software line by line such as in the VEE software (Hill, 2012).

In previous experiments as well as in the present work, the user can set how long they want to record as well as which channels to watch as well as the frequency that data is collected. Once set up, the Agilent software program will begin reading when the U2356A output signal drops to zero volts, the same trigger that tells the current pulse generator in Hill's previous experiment to fire. Now, the software program takes the voltage readings from two channels on the U2531A, one that measures voltage across the composite sample and one that measures the resistance measurements (Hill, 2012).

In Hill's previous electrical pulse and impact settings, once all hardware was powered on the Agilent measurement manager program could be set to the correct settings. This included selecting a single shot recording mechanism as well as choosing the correct two channels to record resistances during the experiment. Also set was the recording rates and sample size of each channel. The recording rate was set to 10000 times per second and the sample size was set at 500. Lastly, the trigger source for the single shot recording was set for when the source voltage on the Agilent U2356A dropped below its standard five-volt setting and the ready button was pressed to arm the software.

The impact force of the tup insert is measured via a load cell called the tup, also shown in Figure 4.4 A plastic tup is used since electrical measurements are being performed.

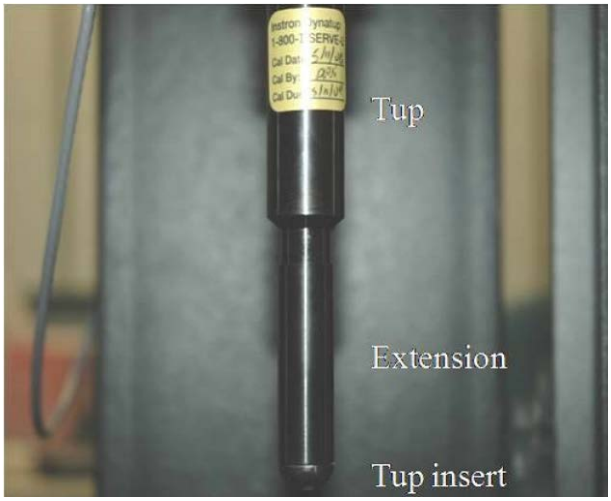

Figure 4.4: Tup, Tup Insert, and Cylindrical Extension (McAndrew, 2009)

To record the impact data, a Dynatup Impulse Version 3 Data Acquisition System is utilized. The data acquisition system was comprised of the following components: the velocity detector, the tup, an Impulse Signal Conditioning Unit (ISCU), a National Instruments (NI) data acquisition card (NI P/N PCI-MIO-16E-1), a computer loaded with Dynatup Impulse Version 3 Software, and the necessary cabling (Instron, 2007). The ISCU is used to magnify the analog output signal from the tup to increase resolution and sensitivity. It also has a second channel to condition the output signal from another source (Instron, 2007). The NI data acquisition card has a resolution of 12 bits and a maximum sampling rate of 1.25 MS/s (National Instruments Corporation, 2003-2005), resulting in a specified 1.17 MHz data sampling rate for the data acquisition system (McAndrew, 2009).

To prevent the tup insert from striking the specimen more than once, the pneumatic rebound brakes (Instron P/N 7820-221) of Figure 4.5 were used.

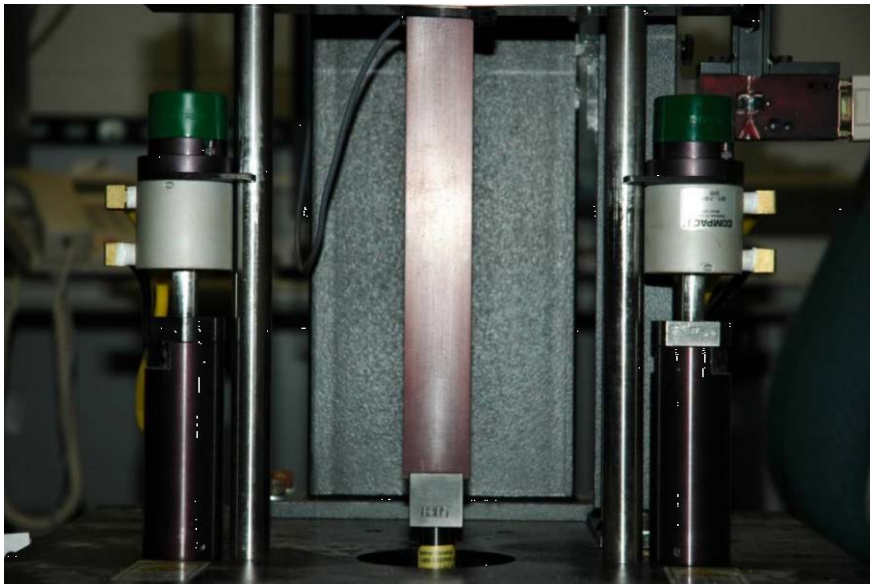

Figure 4.5: Pneumatic Rebound Breaks (McAndrew, 2009)

The cylinders in the brakes extend up after impact to stop the drop weight, thereby preventing any further impacts. Using segmented cylinders known as stop blocks, also shown in Figure 4.5, the initial height of the pneumatic rebound brakes was set (McAndrew, 2009).

4.2.2 New Considerations

In the experimental setup developed in this work, both power supplies are used. The HP 6692A would be used to trigger the pneumatic release of the drop weight and the 6612C Power Supply would be used to supply constant current of 750 mA.

Thus, to test if Power Supply 6692A was still working, the old pulse setup as seen in McAndrew's thesis was modified by using two wires that are connected to the HP 6692A PS and two wires that were connected to the DAQ in order to determine resistance using a 2-wire resistance was instead of the usual 4-wire resistance. Connecting the

oscilloscope wires to the DAQ and using the pulse code written by Wang in VEE Pro, the power supply proved to be producing reasonable data in the Agilent Measurement Manage Test Software. Thus, further modification could be completed.

4.2.3 Modification of Initial Code and Setbacks

In order to set up the coordination of the photogate with resistance measurements, the Agilent Measurement Manage Test U2531A TW4903514 program had to be modified. Since Channel 1 was connected to the pulse generator, it was ignored. Channel 3 is connected to the (DAQ/Power Supply) and Channel 104 is connected to the trigger of the photogate. When the voltage drops from 5 to 0 Volts caused by the top edge of the lower prong passing through the infrared light beam of the velocity detector on the photogate, the voltage drop triggers data acquisition of the resistance measurements.

In order to test the new stage in the setup, the photogate had to be manually triggered, which also corresponds to channel 104 in the program. A new program was initially made by modifying Hill's VEE Pro code to have the photogate be triggered by the Vee Pro program to collect the resistance in Agilent MMT and outsource it to excel.

This new program called "Resistance during Impact" was initially written to try and coordinate both the triggering of photogate to collect resistance values in addition to the Instron DAQ collecting load and impact energies. The initial modification of the code called for combining Hill's VEE Pro code, which allowed for manually setting a constant source current of 750 mA to provide resistances with low uncertainties, with Wang's Pulse VEE Pro code, which had previously allowed for the synchronization of the impact event with current pulse.

However, problems arose in which the VEE Pro could not recognize both power supplies simultaneously due to using the same VISA addresses which made it impossible

to combine both the Hill's and Wang's VEE Pro Codes (Wang, 2012) to make a new program that measured resistance during impact.

One way to rectify this was to instead make the 6692A PS the source that provided constant voltage and manually set the desired current to provide the constant current necessary for simultaneous resistance measurements. The Agilent 6612C PS would resume its previous role to trigger the pneumatic release. However, the 6692A PS did not allow the user to manually set the current as it had controls that dictated that if the current was too low it could not be changed from Direct Voltage to Direct Current (Agilent Manual, 2006). Therefore, creativity had to be used in order to meet the objectives of simultaneous.

4.2.4 Final Setup and Procedure

The final setup used Hill's electrical characterization setup with 6612C PS to constantly supply a current of 750 mA to the composite and the 6692A power supply to trigger the pneumatic system. Two unmodified codes were kept to be manually started, Hill's and Wang's impact VEE Pro code in addition to the modified Agilent Measurement Manager code for simultaneous resistance measurements during impact. The following figures show the final modified setup for resistance and impact testing.

After placing the sample in a test fixture that is clamped securely to the Instron fixture and placing the alligator clips on the probes to measure the electrical resistance in the desired surface, the drop weight assembly could be set to the desired height and impact tests could begin. Using Hill's electrical characterization code, the 6612C PS was turned on in order to manually set the current to 750 mA. Since 6612C PS cannot be recognized in addition to the HP 6692A PS, the GPIB cord connected to Agilent 6612C PS is unplugged yet the power supply is allowed to keep running.

Next, the HP6692A PS is turned on in order to prepare for pneumatic trigger of the Instron Dynatup Model. To prepare for impact, the Wang's impact VEE Pro program is opened and started. At the same time, the Agilent Measurement Manager (AAM) program '1' is started, which waits for channel 104 and the photogate to be tripped in order to start resistance measurements. Going back to Wang's impact program the 'Ok' button is pressed in order to trigger the HP 6692A PS to release the drop weight assembly, triggering the photogate in order for the AAM to collect resistance measurements during impact and the Instron DAQ to collect load and impact data gathered from the tup.

4.2.5 Future Work for Setup Modification

Future work will include looking up how to allow for simultaneous VISA addresses so that both PS can be recognized so there will not be the tedious task of having to unplug the GPIB cord for each measurement. Another improvement can be made in the data analysis by introducing filtering. Data filtering can be done by either writing an excel code to filter the data set or by enabling averaging of channel 3 on the MMT.

4.3 Impact Considerations

It was determined to perform simultaneous impact and bottom resistance measurements as was previously done in the experiments performed by Wang (2012). Thus coordinated impact tests were initially performed at an impact energy of 25 J that was achieved with three 2.22 Kg masses and a height of .38m and tests would be repeated until damage is detected.

4.4 Analysis of Time Coordination between Impact and Resistance Measurements

In the present experimental setup, two different DAQ collected data of impact test and resistance measurement. One of the challenges was to conduct measurements of the resistance during impact tests and find the correspondence between measured impact force and displacement in addition to electrical resistance during the impact tests. For resistance measurements, the difference in time that the top to bottom edge of the flag as it travels through the photogate is determined by finding when the last 0 V appears in the data. The photogate measures the change in signal from 5V to 0V, where the photogate is triggered as the flag moves through the laser in photogate to start recording resistance measurements. When this last 0V data point is found, it is multiplied by 0.0001s since each data point corresponds to time duration of 0.0001s. This time value can then be used to determine the velocity through the photogate using the following relationship:

$$v_1 = \frac{(s_1 - 0.5gt^2)}{t}, \tag{4.1}$$

where t_1 is the time it takes for the flag to pass through the photogate, s_1 is the distance between the top and bottom edge of the flag (s_1 = 0.060 m). Thus, v_1 can now be used to find the time T_2 it takes for the flag to travel from the photogate to the surface of the sample using the following equation

$$T_2 = \frac{-v_1 + \sqrt{v_1^2 + 4s_2 0.5g}}{g}, \tag{4.2}$$

where s_2 (s_2 = 0.074 m) is the distance from when the flag leaves the centerline of the photogate to when the top edge of the flag rests after the drop weight strikes the sample. Next, the total duration of impact must be determined which can be found on the Instron impact software. The time duration, t_3, is found by finding the time corresponding to a deflection of 0 in addition to the time corresponding to the last data point with positive deflection. This is the total time of impact, t_3, which can then be found in the resistance data and added to t_2 to find T_4, which corresponds to a time duration noting the change in the resistance during total time of impact. Thus, the resistance and impact data points can be graphed together to determine correlation.

4.5 Simultaneous Impact and Resistance Results at 25 J

Simultaneous impact and electrical characterization tests were performed on samples 2-8 and 1-8. There was a constant source current of 750 mA applied to the probes on the bottom surface as recommended in Wang's previous simultaneous experiments (Wang, 2012). Seven impact tests were performed on sample 2-8 before change in load was detected in the data. Three graphs showing the load vs. time, deflection vs. time, forces vs. deflection during impact test 6 are seen in Figures 4.6-4.8. Figure 4.9 shows the impact load and resistance plotted together to detect changes in resistance correlated with impact.

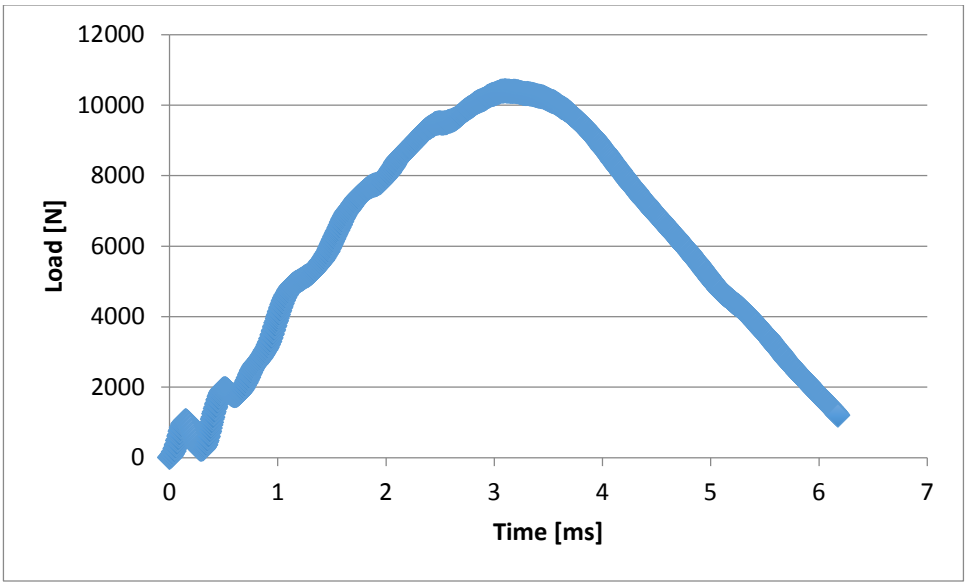

Figure 4.6: Load vs. Time, 6th Impact, Sample 2-8

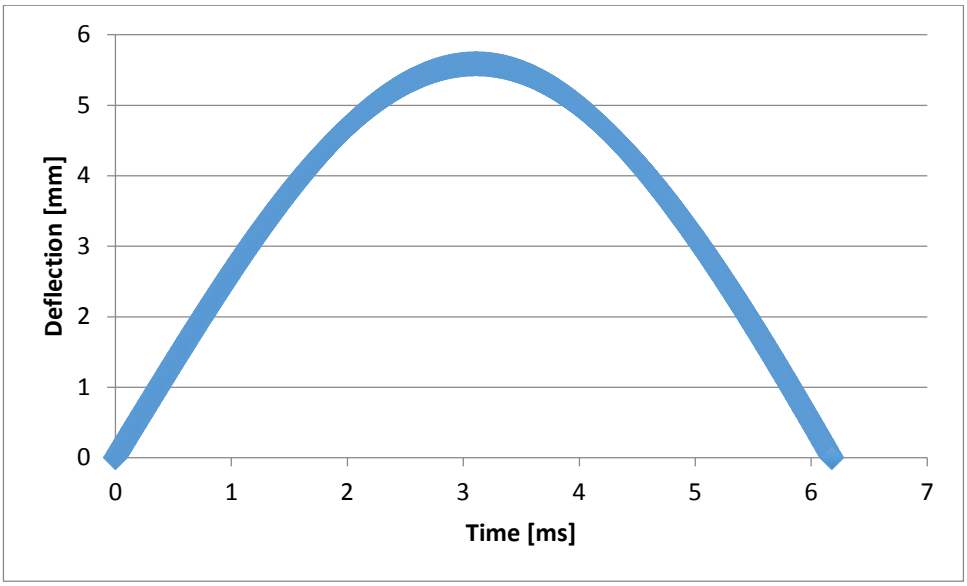

Figure 4.7 Deflection vs. Time, 6th Impact, Sample 2-8

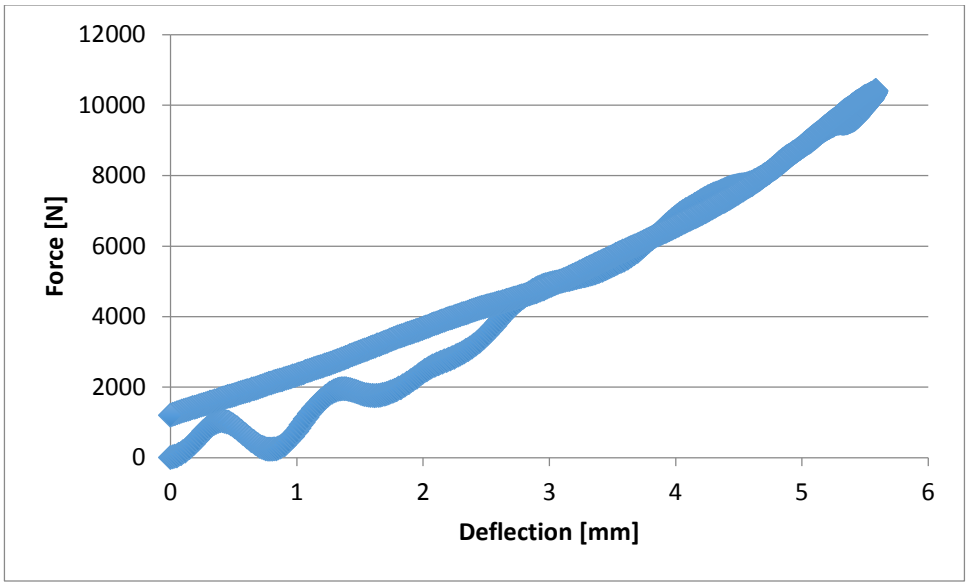

Figure 4.8: Force vs. Deflection, 6th Impact, Sample 2-8

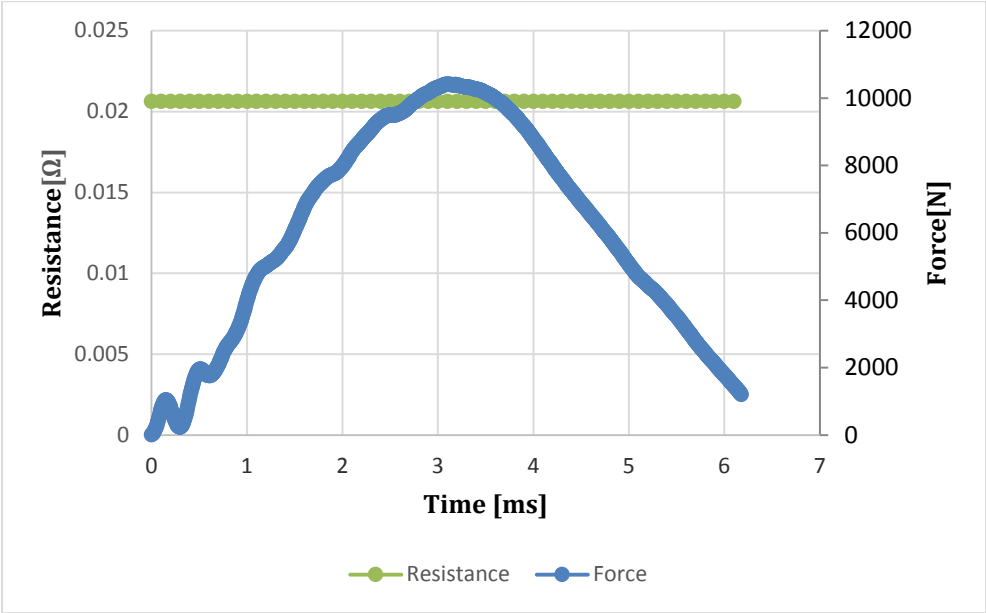

Figure 4.9: Force and Resistance vs. Time, 6th Impact, Sample 2-8

When viewing the force and resistance plotted together it is clear that there is no damage detected nor is there a corresponding change in resistance.

The load vs. time graph in Figure 4.6 shows that some deflection is detected and is seen after the 7th attempt and the results are seen in Figures 4.10-4.13. Figure 4.13 shows the impact load and resistance plotted together to detect changes in resistance correlated with impact.

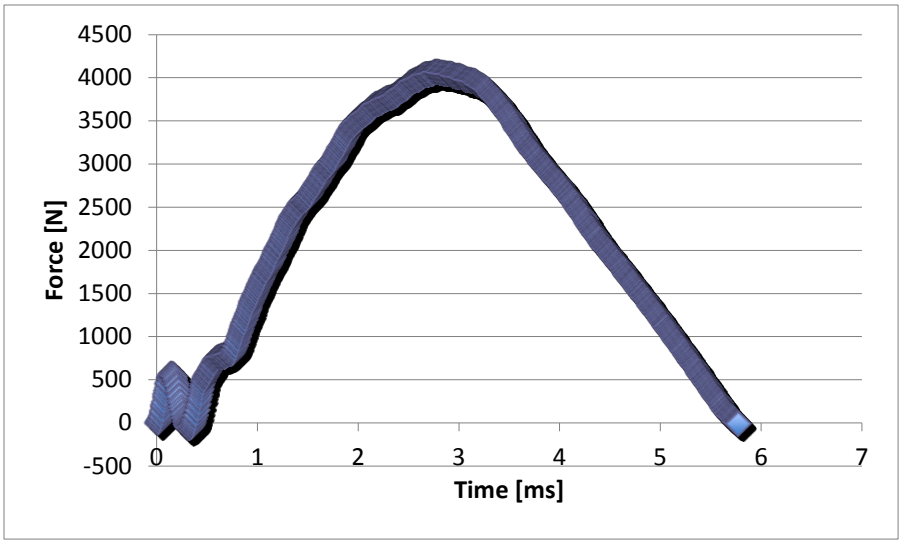

Figure 4.10: Force vs. Time, 7th Impact, Sample 2-8

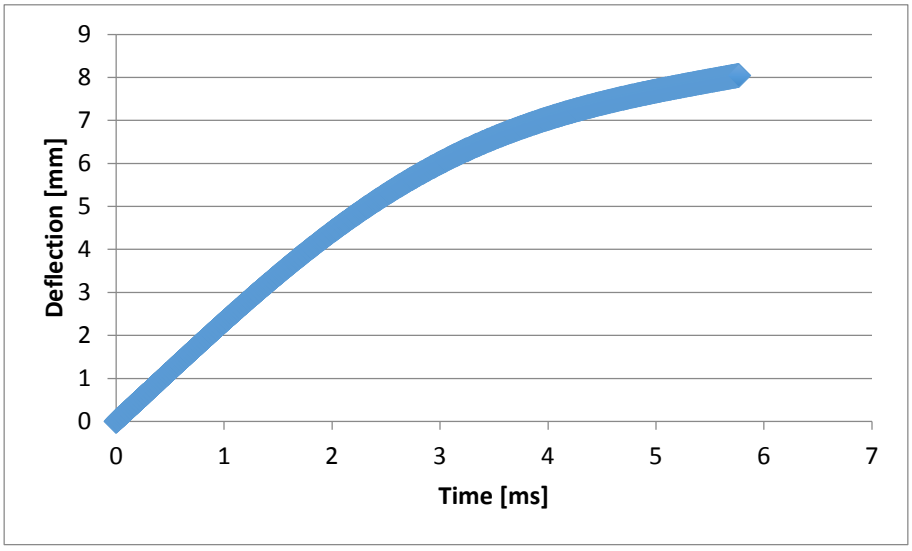

Figure 4.11: Deflection vs. Time, 7th Impact, Sample 2-8

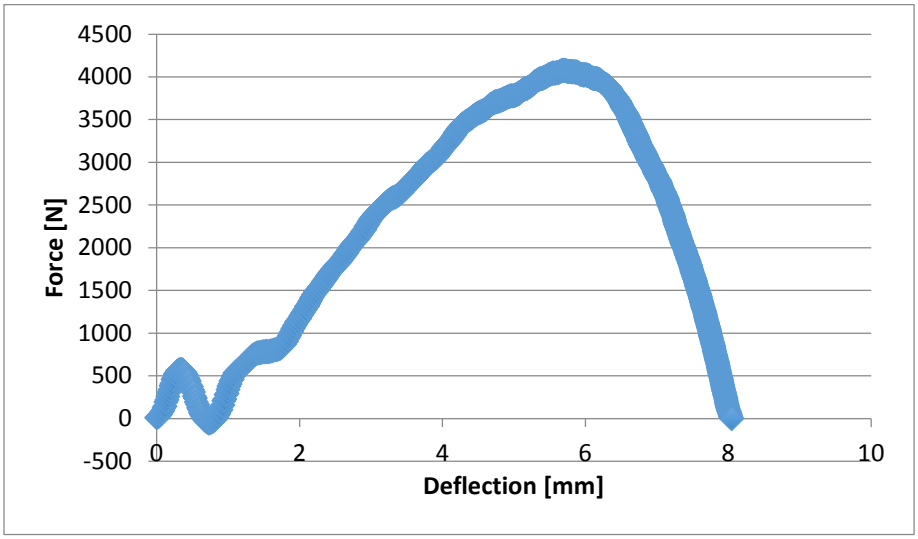

Figure 4.12: Force vs. Deflection, 7th Impact, Sample 2-8

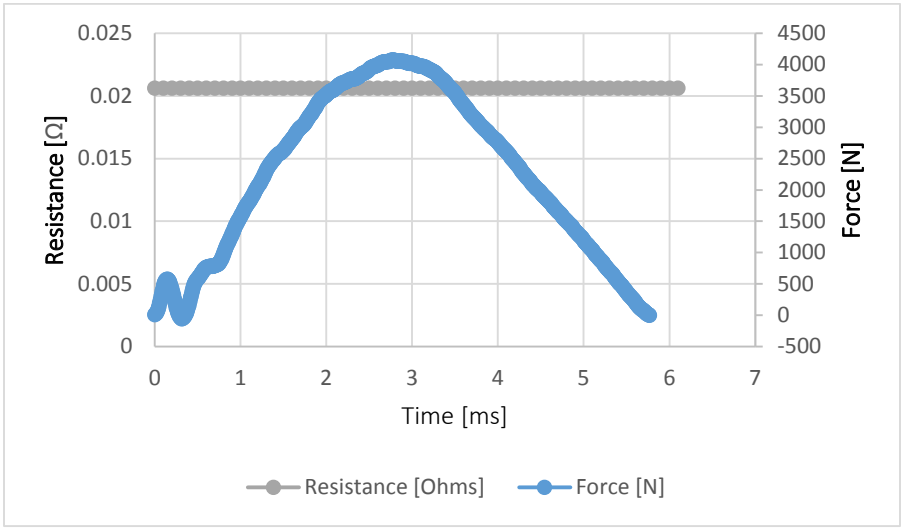

Figure 4.13: Force and Resistance vs. Time, 7th Impact, Sample 2-8

When viewing the force and resistance plotted together it is clear that there is no damage detected nor is there a corresponding change in resistance. It is important to note,

that the 7th attempt shows a decrease in force from 10000 to 4000 N, which indicates that there may be some damage even though it is not visible on the laminate. Top and bottom surfaces of sample 2-8 with no visible damage after 7 impacts are shown in Figures 4.14 and 4.15.

Figure 4.14: Sample 2-8 Top Surface

Figure 4.15: Sample 2-8 Bottom Surface

Nevertheless, as seen in Figure 4.13, the resistance stays constant even during impact with no correlation between impact load and resistance. Furthermore, Table 4.1 shows the resistance history with the initial average resistance before any impact tests taken from Table 3.12 and the constant resistance that was obtained during impact 6 and 7 to see the change in resistance.

Table 4.1: Impact Test
vs. Average Resistance

Impact Test	Resistance [Ω]
No Impact	0.02938
6th	0.02063
7th	0.02063

As seen in the Table 4.1, the average resistance before any impact tests were conducted is higher than the resistances obtained after the 6th and 7th impact tests are performed which does indicate that impact does lower the resistance; yet there is still difficulty in correlating whether this change occurs during impact. It is noted that the resistances of impacts 6 and 7 remained constant throughout the impact whereas the resistance in which no impact occurred is an average. Thus, a total of 7 impacts were performed on sample 2-8.

Impact and resistance measurements were also performed on sample 1-8. Two tests were performed; however, although damage was detected in the first impact test the resistance measurements were not recorded during the impact test due to a lower sampling rate. Thus, only the 2nd impact test for resistance is included.

Figures 4.16-4.18 show the load, deflection, and load vs. deflection for the 1st impact test.

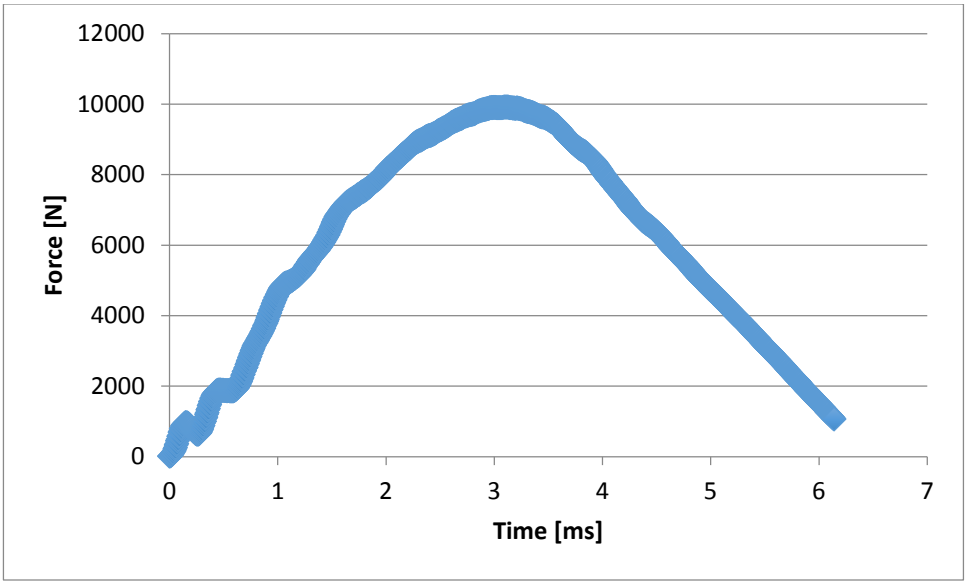

Figure 4.16: Load vs. Time, 1st Impact, Sample 1-8

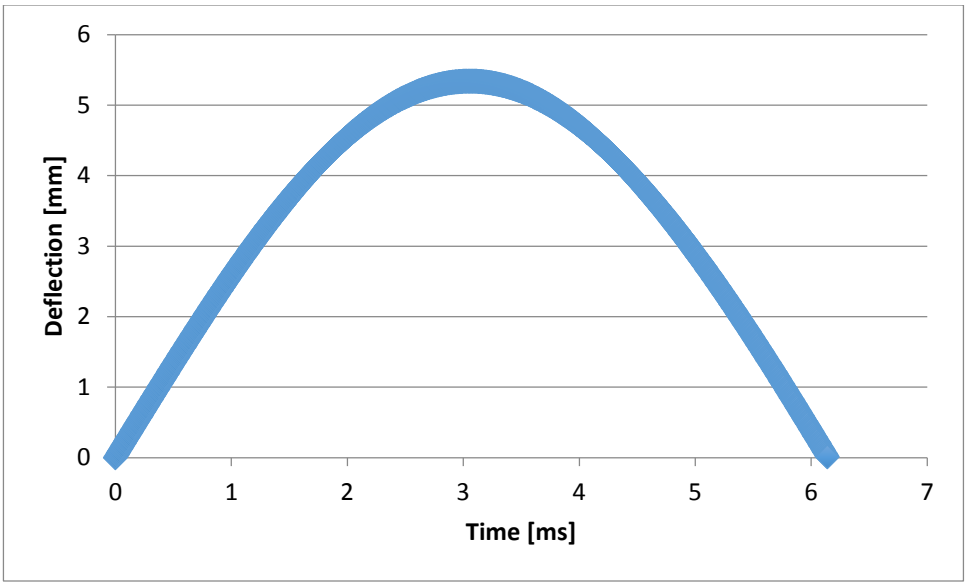

Figure 4.17: Deflection vs. Time, 1st Impact, Sample 1-8

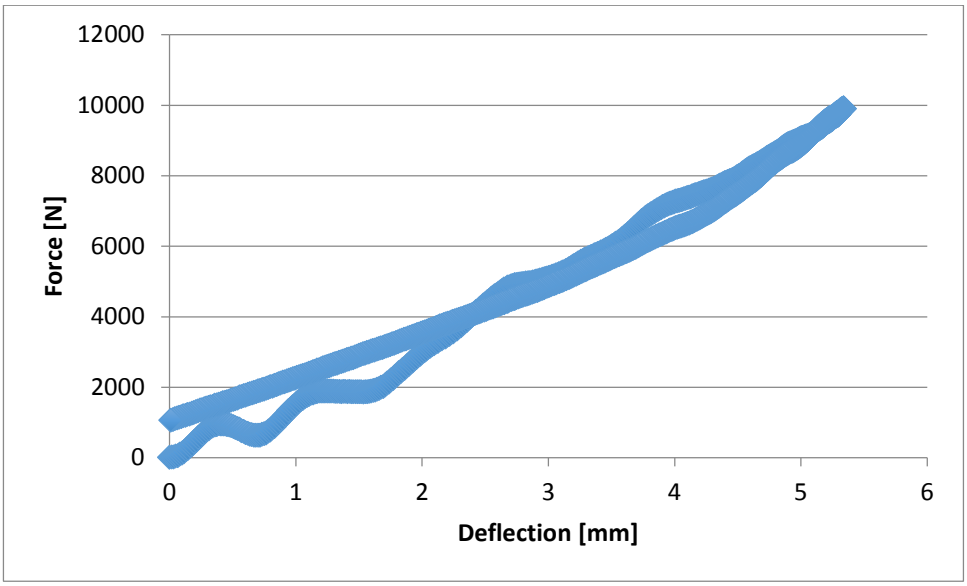

Figure 4.18: Force vs. Deflection, 1st Impact, Sample 1-8

Some deflection after the 1st test is detected but verified by the 2nd test when there is an immediate reduction in load. The graphs are seen in Figures 4.19-4.22. Figure 4.22 shows

the impact load and resistance plotted together to detect changes in resistance correlated with impact.

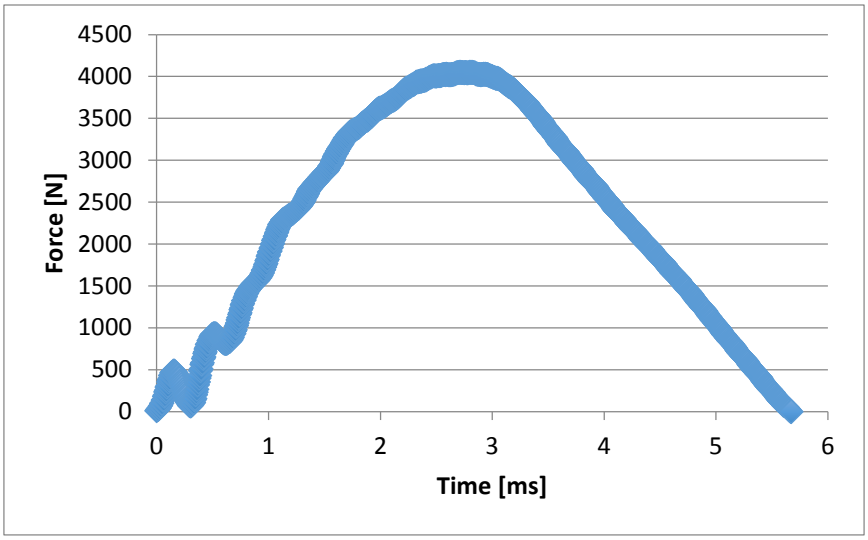

Figure 4.19: Load vs. Time, 2nd Impact, Sample 1-8

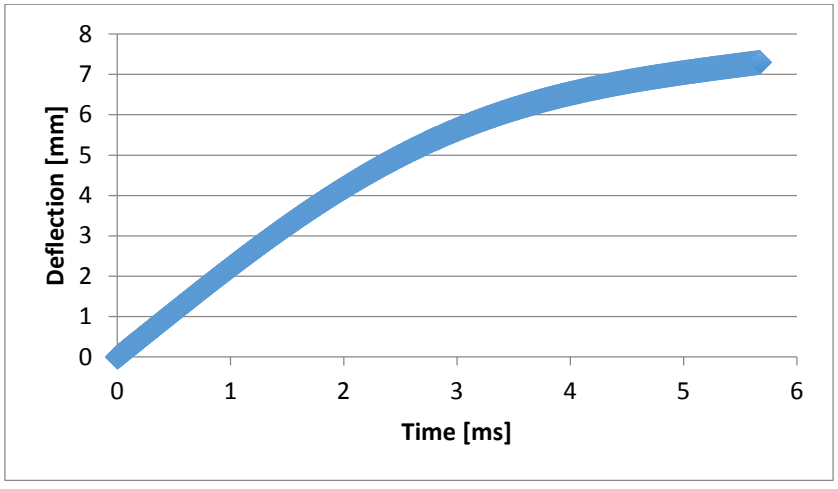

Figure 4.20: Deflection vs. Time, 2nd Impact, Sample 1-8

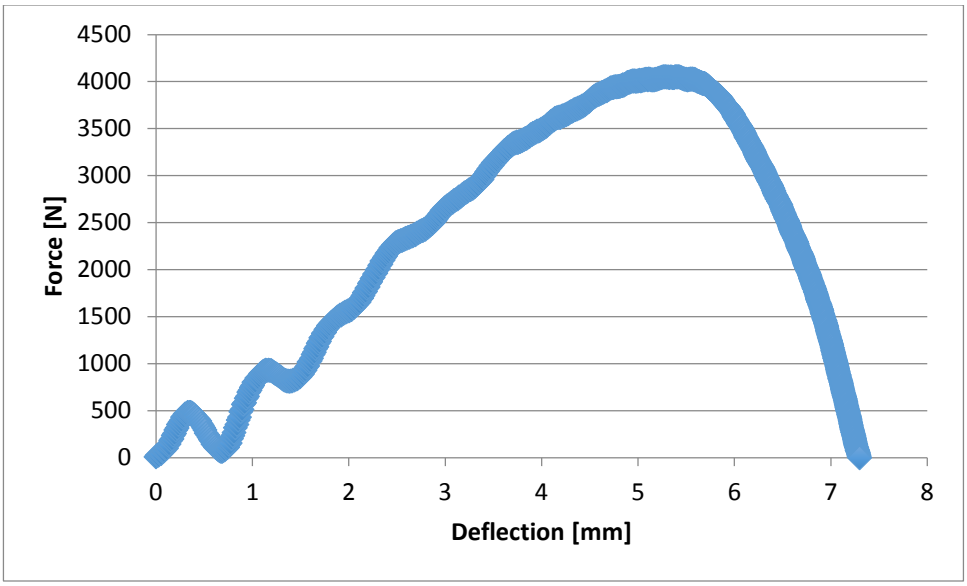

Figure 4.21: Force vs. Deflection, 2nd Impact, Sample 1-8

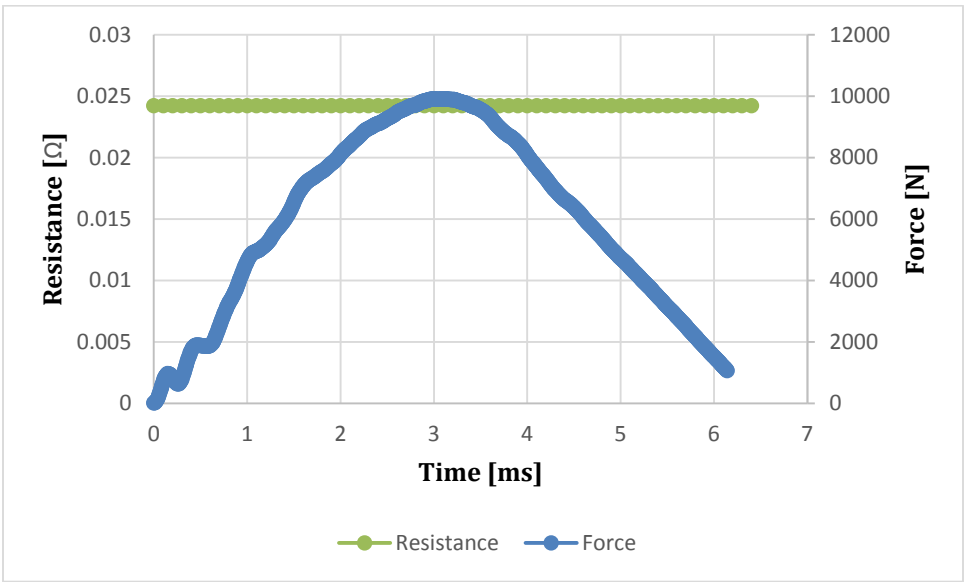

Figure 4.22: Force and Resistance vs. Time, 2nd Impact, Sample 1-8

Internal damage is evident by the decrease in the maximum impact load from 10000 to 4000 N between the 1st and 2nd impact tests in addition to the shape of deflection curve. Again, however, resistance stays constant throughout the duration of impact. Table 4.2

shows the initial resistance values taken from Table 3.12 with no impact vs. the resistance after the 2nd Impact.

Table 4.2:Avg Resistances vs.
# of Impacts for Sample 1-8

Impact Attempts	Resistance [Ω]
No Impact	0.03025
2nd Attempt	0.02423

As seen in Table 4.2, there is a large reduction in the average resistance taken before impact to the constant resistance recorded after impact tests have been performed. The resistance measurements were taken in December 2013 as seen in Table 3.11 and the resistance values after impact were completed in January 2014. The average taken at the 2nd Attempt was constant resistance with no change in resistance during impact. There is evidence that the resistance is reduced after impact but still no correlation can be found whether this change occurs during impact.

Despite of the reduction in the maximum impact load, there was no visible damage observed on the surface of the sample 1-8 after two impacts (see Figures 4.23 and 4.24).

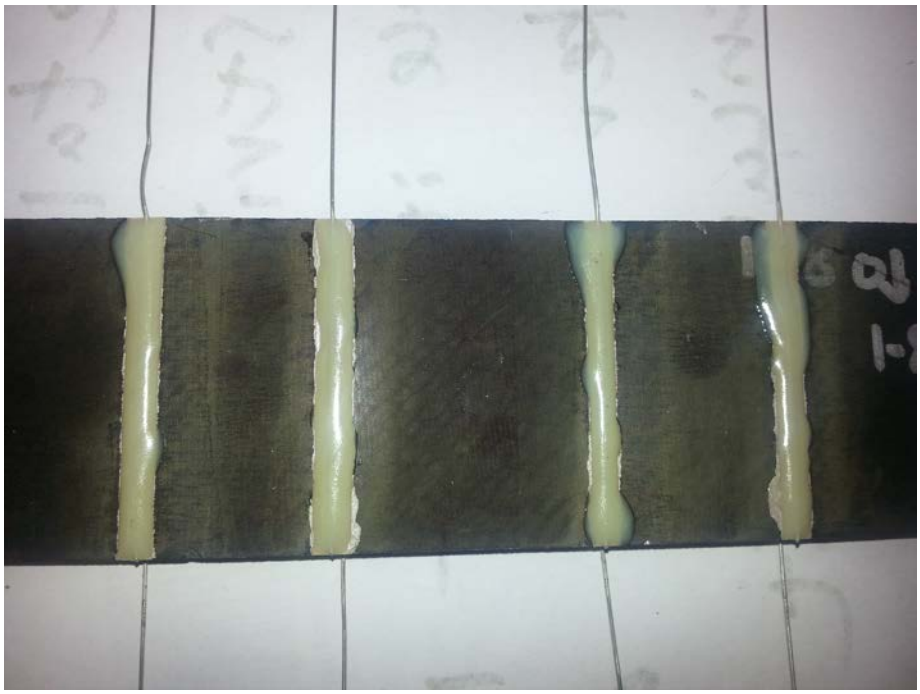

Figure 4.23: Sample 1-8 Top Surface after 2nd Impact

Figure 4.24: Sample 1-8 Bottom Surface after 2nd Impact

There is also no de-bonding between the electrode probes and the laminate on either the top and bottom surfaces. Although there is no visible damage on both samples' surfaces, the data suggests that damage has occurred although possibly internal. CT scans would help to visualize the damage.

With no visible damage and no change in the resistance at the bottom surface, it was decided to perform impacts at impact energy of 28 J and measure the resistance through the oblique surface instead of the bottom. After 4 additional impacts for a total of 14 impacts on sample 2-8, the bottom panel of the wooden fixture broke. In addition, although the fixture broke, there was still no perforation and still no change in resistances corresponding to impact. It was determined to increase the impact energy to 35 J with new test fixture.

4.6: Impact and Resistance Measurements of Oblique Surfaces at 35 J

A new test fixture was manufactured out of PVC to provide for better fixture resistance against impact while being non-conductive. This is seen in Figure 4.25. Due to 0.25" being added to the bottom of the PVC fixture, the zero point of the drop weight had to be moved by moving the ruler to where the drop weight rests on the composite surface.

Figure 4.25: New PVC Test Fixture

From there, the electrical resistance measurements of sample 2-8 through the oblique surface could be continued at an impact energy of 35 J. This energy was calculated by adding one more mass of 1.07 kg to get a total mass of 7.74 kg at a height of 0.46 m. The weight had to be changed on the Instron program to reflect this added weight in the impact energy calculations. Therefore, the sample was connected to the power supply for electrical characterizations.

However, after the first impact at 35 J, the center electrical leads on the top and bottom broke off after impact yet there was no visible damage on the composite surface. The results for the impact are seen in Table 4.3.

Table 4.3: Sample 2-8 Impact Energy of 35 J

Deformation at Peak Force-1 (mm)	Energy to Peak Force-1 (J)	Total Penetration Energy-1 (J)	Failure Force-1 (N)	Failure Deformation-1 (mm)	Failure Energy-1 (J)	Test Velocity-1 (m/s)	Total time-1 (ms)	Energy to max load-1 (J)	Impact energy-1 (J)
3.6013	23.0668	11.1815	2812.8	1.699	13.5788	2.9369	5.6213	23.0668	33.3794

The resistance values did not change and stayed constant at 0.03189 Ω throughout the impact. The maximum energy before electrode detachment was 33.379 J.

Before continuing with further impacts, it was determined to lower the impact energy on an older sample, such as sample 1-8, with impact energy of 30 J to check how much damage it would introduce and determine if this energy level would also lead to the detachment of the electrodes. Again only one impact test was performed before two electrodes broke off as well. The resistance measurements were unable to be captured. Figure 4.26 shows the broken electrodes on Samples 1-8 and 2-8.

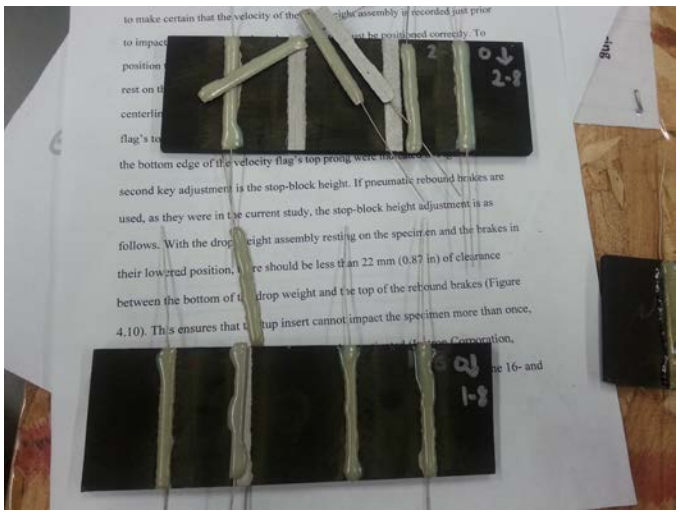

Figure 4.26: Broken Electrodes on Samples 1-8 and 2-8

With the electrodes breaking off it was hard to determine whether the variation in resistance is due to impact or movement in the probes. It is important to note that previous impacts had been conducted on both samples. However, with the wooden fixture there had been no electrode detachment until the PVC fixture was used. Therefore, it was initially thought that the PVC material in the fixture may be too strong and was not absorbing the impact and allowing for as much deflection as the wooden fixture had previously allowed. However, upon further inspection, it was determined that there were too many supports on the test fixture and that was preventing the impact energy needed to perforate the sample. Therefore, an older fixture with little support had to be used.

4.6.1 Impact and Resistance Measurements Sample 1-7 at 25 J

It was determined that since there are too many supportive elements on the previous fixtures (the wooden fixture and the new PVC fixture), an older fixture with no supports was used to allow for clamping of both ends of the sample over a square hole. The previous fixture is seen in Figure 4.29. An older support fixture was used to see if this would produce visible damage along with monitoring electrode damage after impact. Although there were original concerns that a clamped sample would produce bending in the composite, it was determined that with the given fiber direction in this composite, the stiffness would negate bending concerns and perforation was more important. This is seen in Figure 4.27.

Figure 4.27: Older Test Fixture

Impact energy of 25 J was performed on the sample. Three impacts were performed on February 13th, 2014, on sample 1-7 at impact energy of 25 J with simultaneous electrical characterization. Three impacts were performed to examine the load and deflection on the composite that was now clamped on two sides instead of the previous fixture, which had too many supports to facilitate perforation. Thus impact was carried out with the new fixture and clamping setup.

After the first impact was conducted, the left innermost top surface electrode became loose but did not completely fall off. The experiments were continued even as the electrodes that were measuring oblique surface resistances were not affected. Still no visible damage was detected and due to problems with the MMT program, the resistance was not recorded. The load and energy are graphed below in Figures 4.28, 4.29, and 4.30.

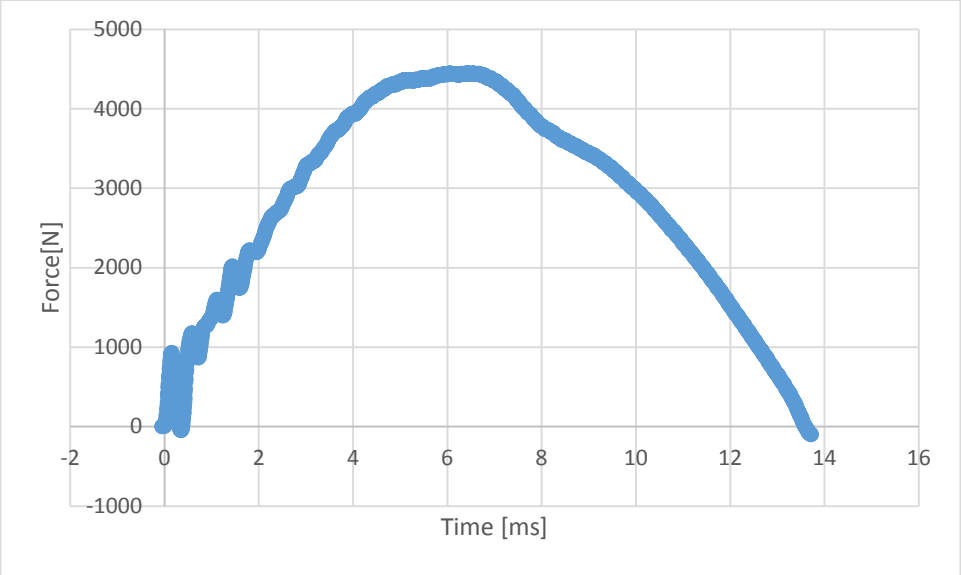

Figure 4.28: Load vs. Time, 1st Impact, Sample 1-7

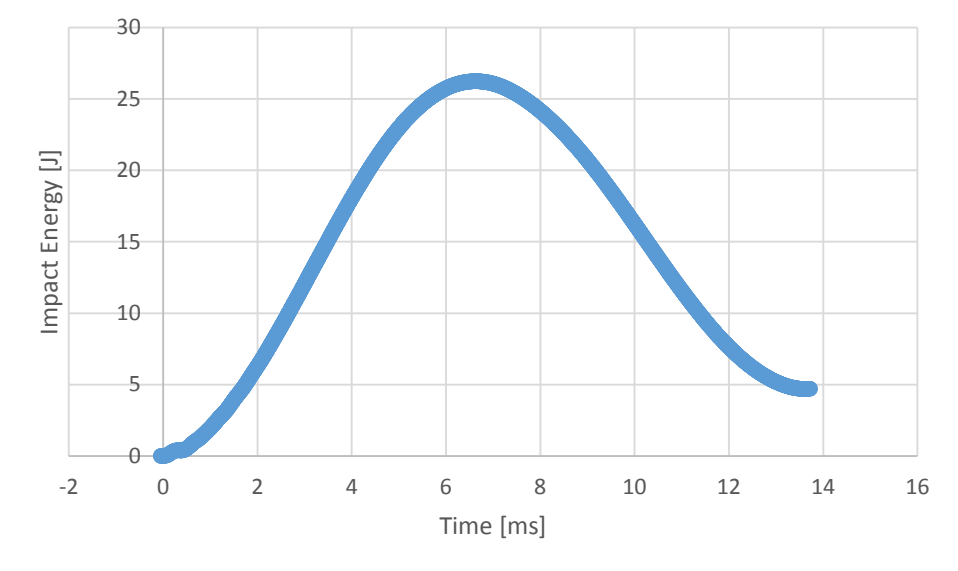

Figure 4.29: Energy vs. Time, 1st Impact, Sample 1-7

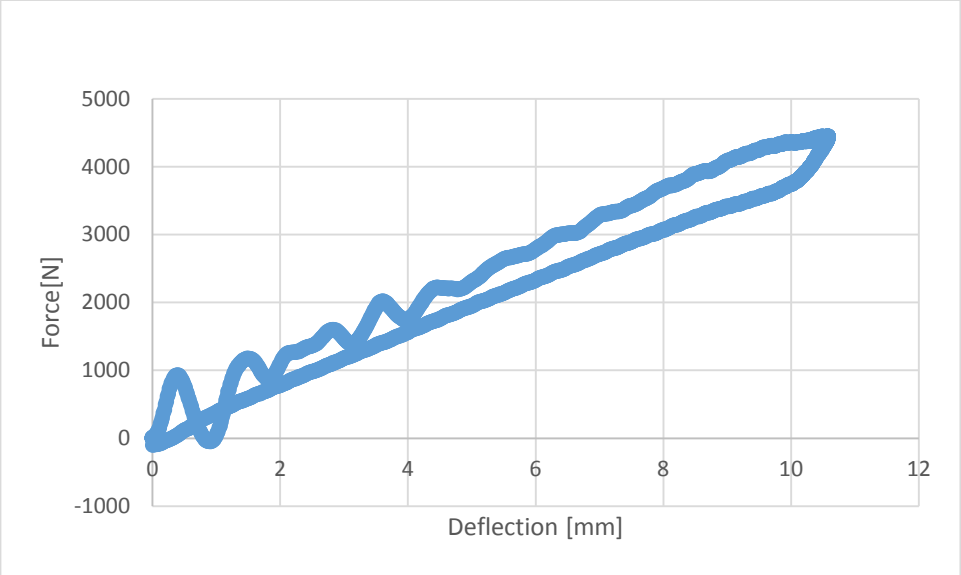

Figure 4.30: Load vs. Deflection, 1st Impact, Sample 1-7

During the 2nd impact, the right innermost top surface electrode became undone with attached alligator clip that was supplying DAQ voltage. Still no visible damage detected and no change in resistance. Due to miscommunication the impact energy was not recorded for this impact.

During the 3rd impact the right innermost top surface electrode came completely off and the left innermost top surface electrode also was damaged during impact and thus resistance could not be recorded as again there was program error. However, the impact energy, load and deflection were recorded in Figures 4.31-4.33 and the max load is 4000 N. Again no visible damage was detected.

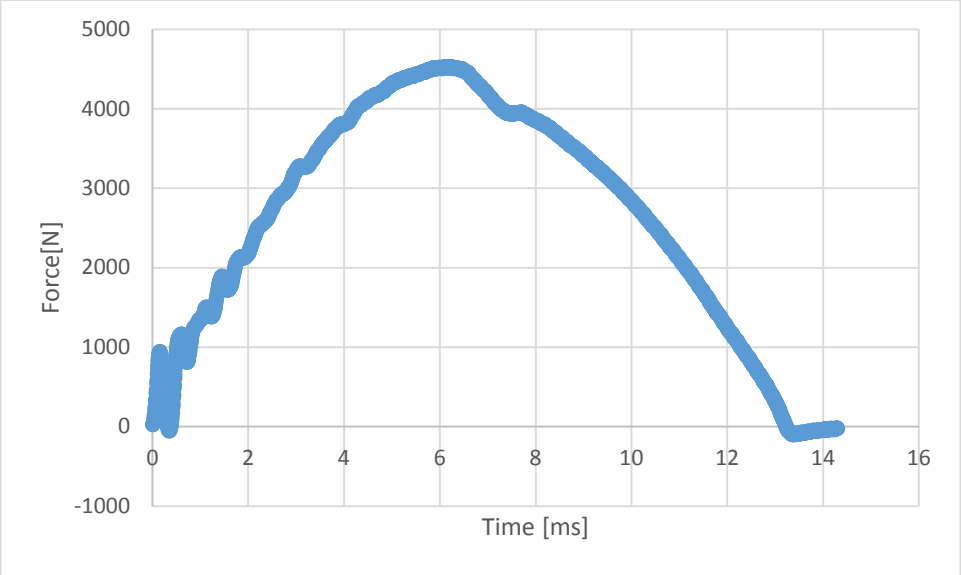

Figure 4.31: Force vs. Time, 3rd Impact at 25 J

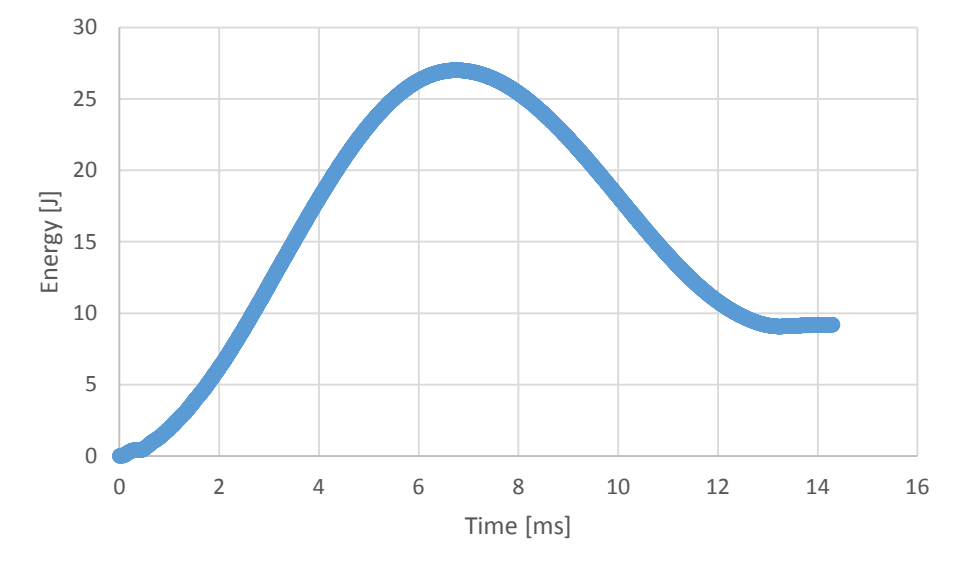

Figure 4.32: Energy vs. Time, 3rd Impact at 25 J

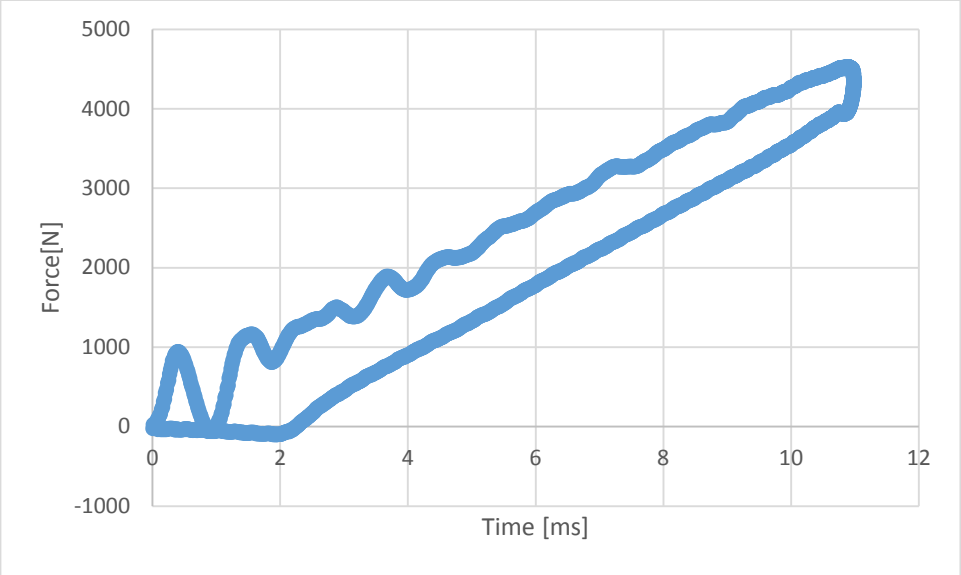

Figure 4.33: Force vs. Deflection, 3rd Impact at 25 J

The sample is seen after the 3rd impact in Figure 4.34.

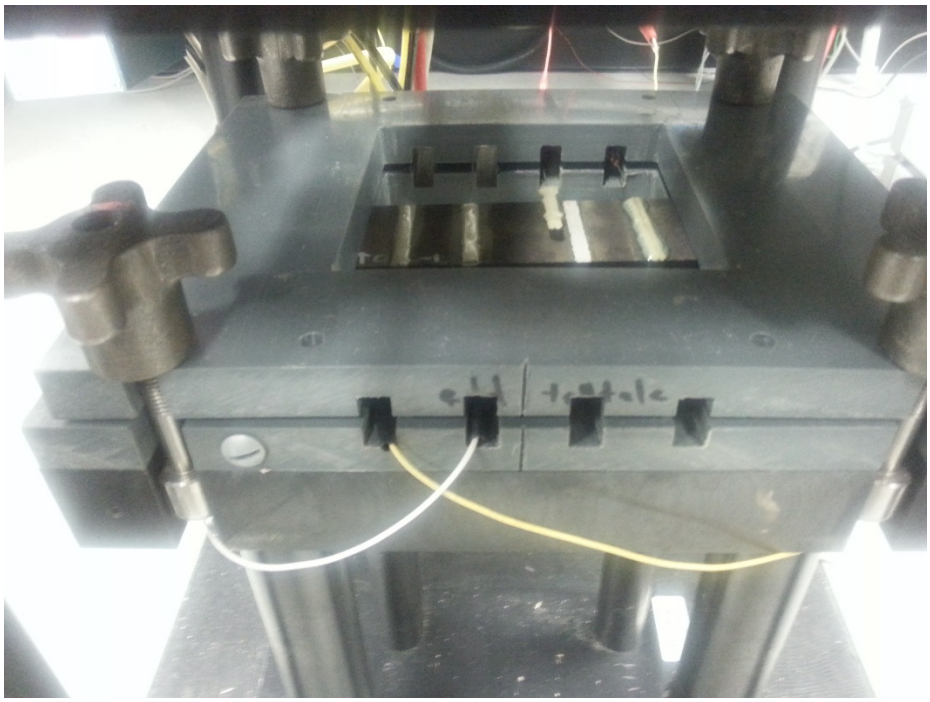

Figure 4.34: Sample 1-7 after 25 J Impact

No further tests were done during that experimental setup due to electrode damage.

Since the fixture and current setup does not allow for impact without damaging the electrodes, more emphasis was put on trying to determine the impact energy needed to perforate the sample rather than electrical characterization tests. Therefore, 4 more impact tests on Monday February 17th, 2014, at 25 J and no perforation was detected. The results are seen in Table 4.4.

Table 4.4: Sample 1-7 February 17th Impact Energy of 25 J

Trial Number (for 2/17/14)	Deformation at Peak Force-1 (mm)	Energy to Peak Force-1 (J)	Total Penetration Energy-1 (J)	Failure Force-1 (N)	Failure Deformation-1 (mm)	Failure Energy-1 (J)	Test Velocity-1 (m/s)	Total time-1 (ms)	Energy to max load-1 (J)	Impact energy-1 (J)
1	10.8284	26.2131	8.4689	902.3	3.8915	9.3517	2.5298	13.2446	26.2131	24.7675
2	10.772	26.1281	8.6273	908.2	3.8956	9.4917	2.5328	13.208	26.1281	24.8271
3	10.9058	26.4971	9.7299	903.4	4.2698	10.5893	2.5532	13.1897	26.4971	25.2285
4	10.8986	26.6844	10.3928	909.1	4.4446	11.2458	2.5603	13.1042	26.6844	25.3691

4.6.2 Impact and Resistance Measurements Sample 2-7 at Higher Impact Energies

As the electrodes began to become damaged, resistance was no longer collected; instead, effort was made to determine the impact energy needed to cause visible sample damage. Therefore, impact experiments were performed at three higher impact energies

of 30, 35, and 45 J The impact energy was then changed to 30 J at a height of 0.395 m. After 10 impacts no visible damage was produced. The results are seen in Table 4.5.

Table 4.5: Results for 30 J on Sample 1-7

	Deformation at Peak Force-1 (mm)	Energy to Peak Force-1 (J)	Total Penetration Energy-1 (J)	Failure Force-1 (N)	Failure Deformation-1 (mm)	Failure Energy-1 (J)	Test Velocity-1 (m/s)	Total time-1 (ms)	Energy to max load-1 (J)	Impact energy-1 (J)
1	11.4036	28.816	20.474	925.4	7.5923	21.1923	2.7577	12.4146	28.816	29.4302
2	11.4031	28.7123	20.2115	922.9	7.5212	20.9215	2.753	12.439	28.7123	29.3303
3	11.2835	28.2996	19.1472	915.1	7.1697	19.8645	2.7256	12.4939	28.2996	28.7496
4	11.389	28.6167	20.0025	914.6	7.4722	20.7119	2.7408	12.4573	28.6167	29.0704
5	11.4294	28.698	20.8486	924.3	7.7671	21.5641	2.7592	12.4084	28.698	29.4636
6	11.4272	28.6398	20.9197	924.3	7.8064	21.6242	2.7572	12.3962	28.6398	29.42
7	11.4295	28.6087	20.9812	925.2	7.828	21.6821	2.7591	12.3901	28.6087	29.4611
8	11.4734	28.774	20.687	925.2	7.7331	21.4069	2.7612	12.439	28.774	29.5062
9	11.3629	28.4561	19.6227	921.3	7.3595	20.3551	2.738	12.5061	28.4561	29.0125
10	11.4453	28.7802	20.3448	925.7	7.6016	21.0756	2.7534	12.4573	28.7802	29.3393

The impact energy was increased to 35 J at a height of 0.46 m and again after 8 impact tests were performed, there was still no visible damage on the surfaces. The results are seen in Table 4.6.

Table 4.6: Results for 35 J on Sample 1-7

	Deformation at Peak Force-1 (mm)	Energy to Peak Force-1 (J)	Total Penetration Energy-1 (J)	Failure Force-1 (N)	Failure Deformation-1 (mm)	Failure Energy-1 (J)	Test Velocity-1 (m/s)	Total time-1 (ms)	Energy to max load-1 (J)	Impact energy-1 (J)
1	11.7828	30.4062	25.6735	941.1	9.1768	26.3128	2.8762	12.0789	30.4062	32.0156
2	12.1939	32.1843	29.133	950.3	10.2109	29.7095	2.9615	11.8896	32.1843	33.9422
3	12.2548	32.3186	29.9114	956	10.4824	30.4866	2.9812	11.8408	32.3186	34.3959
4	12.2251	32.4832	29.8923	951.2	10.403	30.4561	2.9802	11.8225	32.4832	34.3706
5	12.268	32.4782	30.2834	945.9	10.5683	30.8348	2.9869	11.8103	32.4782	34.526
6	11.9341	30.934	30.392	946.4	10.5789	30.9336	2.9904	11.7981	30.934	34.6073
7	12.2756	32.5028	30.3751	956.5	10.6033	30.9334	2.9901	11.8042	32.5028	34.5996
8	12.2561	32.3445	30.1868	956	10.5817	30.7507	2.9818	11.8103	32.3445	34.4086

Ten impacts were then performed at 45 J at a height of 0.521m with a new mass of 8.81 kg (5 blocks). At the 5th impact, a loud crack was heard. Upon inspection, it was determined that the final electrode that was more securely affixed to the composite had broken off yet there was still no visible damage on the top or bottom surface. The graph denotes a change in the load as seen in Figure 4.35.

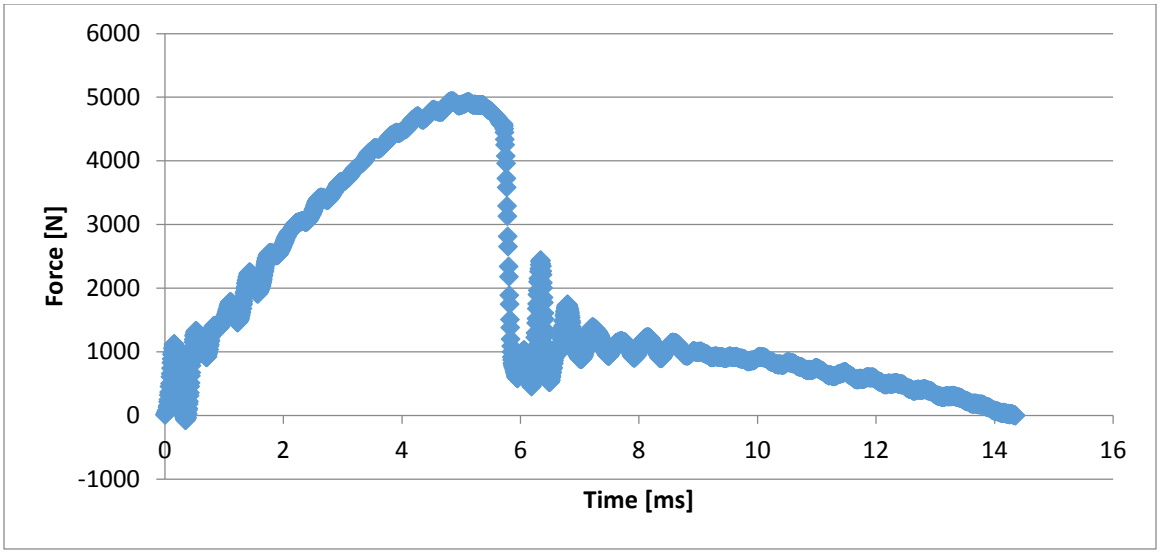

Figure 4.35: Sample 1-7, Impact Energy 45 J, 5th Impact

From the graph, it was determined that there was significant internal damage although no visible damage was seen. Five more impacts we conducted to achieve 10 total impacts. Although no surface damage was detected after the 10th impact, 5 more were conducted due to the change in deflection. The total results 15 impacts at 45 J are seen in Table 4.7.

Table 4.7: Results for 45 J on Sample 1-7

	Deformation at Peak Force-1 (mm)	Energy to Peak Force-1 (J)	Total Penetration Energy-1 (J)	Failure Force-1 (N)	Failure Deformation-1 (mm)	Failure Energy-1 (J)	Test Velocity-1 (m/s)	Total time-1 (ms)	Energy to max load-1 (J)	Impact energy-1 (J)
1	12.5409	34.0997	34.2328	980.7	11.4375	34.7681	3.1279	11.7432	34.0997	37.8622
2	12.184	32.4751	34.5749	981.2	11.5025	35.102	3.1374	11.7188	32.4751	38.0938
3	12.4814	33.8226	34.7156	981.2	11.575	35.2547	3.1422	11.7126	33.8226	38.2102
4	12.2498	32.5598	34.5147	981.2	11.5495	35.0525	3.1355	11.731	32.5598	38.0476
5	12.2581	32.554	40.4453	921.8	13.3763	37.748	3.147	14.3494	32.554	38.3274
6	14.6916	17.0033	32.345	376.6	28.0063	31.9705	3.1275	13.3972	17.0033	37.8533
7	14.7635	17.0645	32.3585	381.6	28.0186	31.9612	3.1284	13.4277	17.0645	37.8745
8	14.7494	17.1595	32.7177	386.7	28.1109	32.2971	3.15	13.3972	17.1595	38.3999
9	14.7096	16.9568	32.5851	386.3	28.179	32.1813	3.1457	13.3972	16.9568	38.2953
10	14.9285	17.3938	32.7069	386.5	28.1706	32.2992	3.1449	13.4583	17.3938	38.2764
11	14.9006	17.4661	32.7459	386.9	28.2386	32.3618	3.1477	13.446	17.4661	38.3446
12	14.801	17.176	32.6992	381.6	28.2478	32.3084	3.1503	13.4094	17.176	38.4071
13	14.7239	17.0348	32.6463	386.5	28.1455	32.2326	3.1473	13.3911	17.0348	38.3344
14	14.7541	17.1249	32.7906	386.3	28.2294	32.3884	3.1546	13.385	17.1249	38.5122
15	14.9051	17.2706	32.7002	391.3	28.1993	32.2693	3.1511	13.4033	17.2706	38.4275

As seen after impact 5, there is a significant increase in deformation and failure deformation at peak force in addition to a reduction in failure force, which indicates significant damage. Although no visible surface perforation was detected, upon taking

out the sample out of the fixture it was determined that there was massive delamination in the center layers of the composite. The damage is seen in Figures 4.36-4.39.

Figure 4.36: Side 1 Delamination of Sample 1-7

Figure 4.37: Delamination Side 2 of Sample 1-7

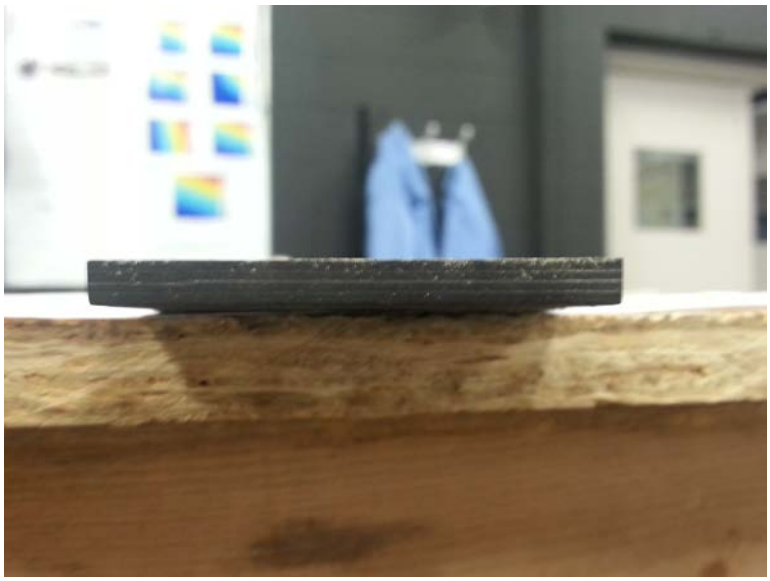

Figure 4.38: Delamination Side 3 of Sample 1-7

Figure 4.39: Delamination Side 4 of Sample 1-7

Thus, the force results really indicate that it was as if the drop weight was hitting two separate composite samples. Since it was determined that one would break the electrodes before damaging the composite, further experiments were conducted on wider

6” x 6” composite samples to determine the impact and resistance within a wider sample composite.

4.7 Impact Measurements on Wider Samples

Multiple impacts were conducted at different impact energies on the wider panels to determine at what energy level wider samples would become damaged and try to attempt simultaneous resistance measurements on the wider samples to determine whether there is a correlation between damage and resistance.

The tests were performed using the same setup as the horizontal beams yet a different fixture to allow for the larger sample. Based on results from Song (2013) experimental results on the larger samples where visible damage was seen around 22 J, it was determined to start at an impact energy of 14 J. A fixture with no supports was used and a drop weight of 6.67 kg was also used.

Initially, resistance measurements were conducted to capture resistance before impact, during impact, and after impact. However, it was determined that due to the placement of the power supplies near the oscilloscope that would signal the photogate to capture simultaneous resistance measurements during impact, there was noise introduced into the resistance measurements. Trying to rectify the situation by moving the power supplies proved fruitless as noise was still being introduced. Thus, the setup does not allow for simultaneous resistance measurements. Instead, the experiments were refocused on determining change in resistance due to increasing the size of the samples from smaller beams to wider horizontal samples by capturing resistance measurements before and after impact. More importantly, trying to determine the impact energy that causes visible damage and analyzing the resistance changes before and after this event was a priority.

Thirty-four resistance measurements and impacts were taken on sample 1-1 of the wider composite sample. Since there was concern on breaking the electrodes, it was determined to focus on taking resistance measurements before and after impact, rather than simultaneously to determine if there was correlation between impact and resistance change in a wider sample. Table 4.8 shows the resistance measurements taken before and after the last impact before changing the impact energy.

Table 4.8: Average Change in Resistance after Impact

Before Impact Number	Energy [J]	Average Resistance [Ω]	Change in Resistance [Ω]
1	14	0.0207997	
17	20	0.0142595	
18	20	0.0179185	0.00365897
27	22	0.0156734	
28	22	0.0161836	0.00051024
33	30	0.0148284	
34	30	0.0148087	-1.97E-05

As seen in Table 4.8, resistance decreases after multiple impacts at higher impact energies, however the change in resistance gets smaller until it gets negligible after the highest impact energy of 35 J is inflicted on the sample. Theoretically, this is due to the fact that while the specimen deforms elastically; compression appears to result in an increase in contact between the fibers which gives rise to the decrease in resistance. The resistance increases drastically; as a result of the removal of the compressive force, the fractures resulting in discontinuities in the fibers should have in effect (Lim et all, 2011).

As explained during the discussion of those results, it is believed that a lack of a direct relationship between impact energy and change in resistance was partly due to the large variation in sample initial resistances. This variation may have been caused by

slight differences in contact placement and/or differences in the microstructure of the samples, such as the percentage of fibers touching (McAndrew, 2009).

With this thesis, however, the textile composites had a much larger resistance than that reported in McAndrew's thesis which may be due to how the current enters the electrically conductive woven fibers. Also, it is to be noted that his impact resulted in failure whereas the natural stiffness of the composite coupled with a fixture with too many supports prevented failure. Theoretically, the resistance is supposed to increase with delamination. Since failure and delamination were unable to be captured with this setup and material, it is hard to correlate changes in resistance with fiber damage and delamination. Table 4.9 shows the impact energies with sample 1-1.

Table 4.9: Impact Energies Sample 1-1

Deformation at Peak Force-1 (mm)	Energy to Peak Force-1 (J)	Total Penetration Energy-1 (J)	Failure Force-1 (N)	Failure Deformation-1 (mm)	Impact energy-1 (J)
4.8465	13.2936	-1.6255	1611.9	1.239	12.897
5.1594	15.4911	-1.1065	1508	1.5755	14.2762
5.0065	17.9227	-2.1772	1735.6	1.253	16.6812
5.1554	19.6834	-2.0425	1795.3	1.2592	18.505
7.3805	15.4331	21.2467	823.6	9.1673	20.2375
6.3531	30.0367	-0.4688	2256.1	1.9035	29.2187
8.7704	31.1735	20.3103	1445.4	5.8702	31.2567

Even after 34 impacts, there was still no visible damage or delamination on the wider sample by the end of the study. This shows that the stiffness of the 45 degree Satin Harness composites is too high for the current setup to break without possibly damaging the electrodes.

CHAPTER 5
SUMMARY AND RECOMMENDATIONS

5.1 Summary

In this work, electrical and impact properties of carbon fiber textile composites were analyzed and compared. This included determining the source current needed to produce accurate four-wire resistance measurements through the top, bottom, and oblique surfaces using setups developed by McAndrew (2009) and Hill (2012). It was determined that a source current of 750 mA produced accurate resistance measurements using Hill's four-wire resistance setup and that the oblique surface held the highest resistance measurements for both beam and square textile carbon fiber samples.

Next was to determine the impact energy that would produce visible damage and modifying Hill's setup to allow for simultaneous resistance measurements through the oblique surface. Theoretically, the resistance is supposed to increase with delamination. Since delamination and simultaneous resistance measurements were unable to be captured with this setup and material, it is hard to correlate changes in resistance with fiber damage and delamination.

It was found that the fixture and setup were also unsuited to capture simultaneous resistance and impact measurements due to too much noise being introduced in the oscilloscope that captures resistance measurements due to instrument placement; in addition, the textile composite beam specimens proved to be too stiff to allow for visible damage that would also allow for the electrodes to be undamaged. It took 35 multiple impacts and an impact energy of 45 J to finally produce delamination of the entire beam composite lamina yet resulted in catastrophic electrode failure.

The same was trouble with stiffness of the material was seen in impact on wider sample 1-1 yet no delamination or damage was able to be inflicted on the sample even

after 35 successive impacts at increasing impact energies. Nevertheless, resistance measurements decreased following non-destructive impacts, which still show the decreasing relationship between impact and resistance change that was seen in Hill (2012) results. Although there is evidence that the resistance is reduced after impact, since no damage occurred where resistance was able to be simultaneously measured, there is still no correlation whether this change occurs during impact. Overall, the results show that the one-dimensional electrical resistance technique had a limited success at sensing impact damage in the textile composites due to high mechanical stiffness and low electrical resistance of the textile laminates.

5.2 Recommendations

Recommendations would include using a composite with a lower stiffness to allow for lower impact energy in order to inflict damage and conduct simultaneous resistance measurements. This could also be accomplished by manufacturing a different fixture with fewer supports on which the composite rests. Although bending is a concern, trying to perforate the sample to determine the relationship between visible damage and change in resistance measurements using a less supportive fixture would be the ultimate goal.

REFERENCES

Abrate, S. (1998). *Impact on Composite Structures*. New York, NY: Cambridge University Press.

Agilent Technologies. (2006). *Agilent 34970A Data Acquisition/Switch Unit User's Guide* (Manual No. 34970-90003). Retrieved January 21, 2009, from Agilent Technologies, Technical Support: 34970A Data Acquisition Switch Unit Web site: http://cp.literature.agilent.com/litweb/pdf/34970-90003.pdf.

Bakar, I. (2013). "Optimization of Elastic Properties and Weaving Patterns of Woven Composites". Composite Structures.

Balaguru, P. Ianni, A. Giancaspro, J. (2009). "FRP Composites for Reinforced and Prestressed Concrete Structures: A Guide to Fundamentals and Design for Repair and Retrofit". Taylor & Francis. Website: http://books.google.com/books?id=RLsFEygpEUUC&pg=PA27&lpg=PA27&dq=carbon+fibers+that+follow+twill+weave+with+warps+and+wefts&source=bl&ots=OM9kdG7CfK&sig=E6QDYN1RC4Aed182OmW38hz6z6g&hl=en&sa=X&ei=MBgcUcStAYr22AXesoCYCA&ved=0CEIQ6AEwAw#v=onepage&q=carbon%20fibers%20that%20follow%20twill%20weave%20with%20warps%20and%20wefts&f=false.

Composite Envisions. (2012). Website: http://compositeenvisions.com/.

Chung, D. D. L. (2007). Damage detection using self-sensing concepts. *Proceedings of the Institution of Mechanical Engineers Part G-Journal of Aerospace Engineering, 221*(G4), 509-520.

Dugmatti. S. et all. (2010). "Local damage in a 5-harness satin weave composite under static tension: Part I – Experimental analysis." *Composites Science and Technology.*

Dugmatti. S. et all. (2011). "Local strain in a 5-harness satin weave composite under static tension: Part I – Experimental analysis". *Composites Science and Technology.*

Dugmatti. S. and Voet, E. (2011). "In-situ local strain measurement in textile composites with embedded optical fiber sensors". *Composites Science and Technology.*

Figliola, R.S. & Beasley, D.E. (2000). *Theory and Design for Mechanical Measurements* (3rd ed.). Hoboken, NJ: John Wiley & Sons, Inc.

Hexcel Corporation. (2010). "Hexcel Aerospace Selector Guide".

Hill, C. (2012). "Investigation of electrical and impact properties of carbon fiber reinforced polymer matrix composites with carbon nanotube buckypaper layers". Thesis. The University of Iowa. Print.

Hill, C. (2011). "Composite Material Damage Analysis through the use of Electrical Resistance Testing". The University of Iowa.

Kim, J. (2004). "Mechanical properties of woven laminates and felt composites using carbon fibers." Composites Science and Technology 64. 2221–2229.

Lim, A. et all. (2011). “Mechanical and electrical response of carbon nanotube-based fabric composites to Hopkinson bar loading.” *Composites Science and Technology.*

Long AC. (2005). “Design and manufacture of textile composites”. Cambridge: Woodhead Publishing Limited.

Instron Corporation. (2005). *Instron Dynatup Model 8200 Drop Weight Impact Testing Instrument Operating Instructions* (M14-14103-EN Revision D).

McAndrew, J. (2009). “Impact damage sensing in carbon fiber polymer-matrix composite plates via electrical resistance measurement”. Thesis. The University of Iowa. Print.

Motahhari, S., Cao, Y. M., & Cameron, J. (2000). Damage evaluation by means of electrical resistivity measurements. *Polymers & Polymer Composites*, *8*(7), 449- 453.

National Instruments Corporation. (2003-2005). *NI 6070E/6071E Family Specifications* (Part number 370725C-01). Retrieved June 11, 2009, from http://digital.ni.com/manuals.nsf/websearch/53C5FF75028D46DB862570A80066 628A.

Richardson, M. O. W., & Wisheart, M. J. (1996). Review of low-velocity impact properties of composite materials. *Composites Part A-Applied Science and Manufacturing, 27*(12), 1123-1131.

Safarova, V and Gregr, J. (2010). “Electrical Conductivity Measurement of Fibers and Yarns” *7th International Conference.* http://wjoe.hebeu.edu.cn/sup.2010/Quality%20Control%20and%20Testing%20in%20Textile%20Branch/20_p_Safarova.pdf.

Sevkat, E. et all. (2008). “A statistical model of electrical resistance of carbon fiber reinforced composites under tensile loading.” *Composites Science and Technology.*

Schulte, K. Baron. C. (1989). “Load and failure analysis of CFRP laminates by means of electrical resistivity measurements”. *Comp. Sci. Technol., 36 (1989), pp. 63–76.*

Song, C. (2013). “Test Report”. The University of Iowa.

Todoroki, A. and Kobayashi, H. (1994). "Application of Electric Potential Method to Smart Composite Structures for Detecting Delamination" Trans. Jpn. Soc. Mech. Eng., V01.60, No.574, A, pp.1458 – 1463.

Ullah, H. Harland, A.R, Lucas, T. Price, D. (2011).“Analysis of Nonlinear Deformations and Damage in CFRP Textile Laminates.” Journal of Physics: Conference Series 305. Website: http://iopscience.iop.org/1742-6596/305/1/012045/pdf/1742-6596_305_1_012045.pdf.

Vieille, B. Bouvet, C. Casado, V.M. (2013). “About the impact behavior of woven-ply carbon fiber- reinforced thermoplastic- and thermosetting-composites: A comparative study”. *Composite Structures, vol. 101. pp. 9-21. ISSN 0263-8223.* Website: http://oatao.univ-toulouse.fr/9328/1/Bouvet_9328.pdf.

Wang, Y. (2012). “Report on Damage Detection Test of FSU Composite Samples One time test”. The University of Iowa.

Weber, I. Schwartz, P. (2001). “Monitoring bending fatigue in carbon-fiber/epoxy composite strands: a comparison between mechanical and resistance techniques” http://www.sciencedirect.com.proxy.lib.uiowa.edu/science/article/pii/S0266353801000288